Ageing of High Energy Density Automotive Li-Ion Batteries: The Effect of Temperature and State-of-Charge

OPEN ACCESS

Ageing of High Energy Density Automotive Li-Ion Batteries: The Effect of Temperature and State-of-Charge

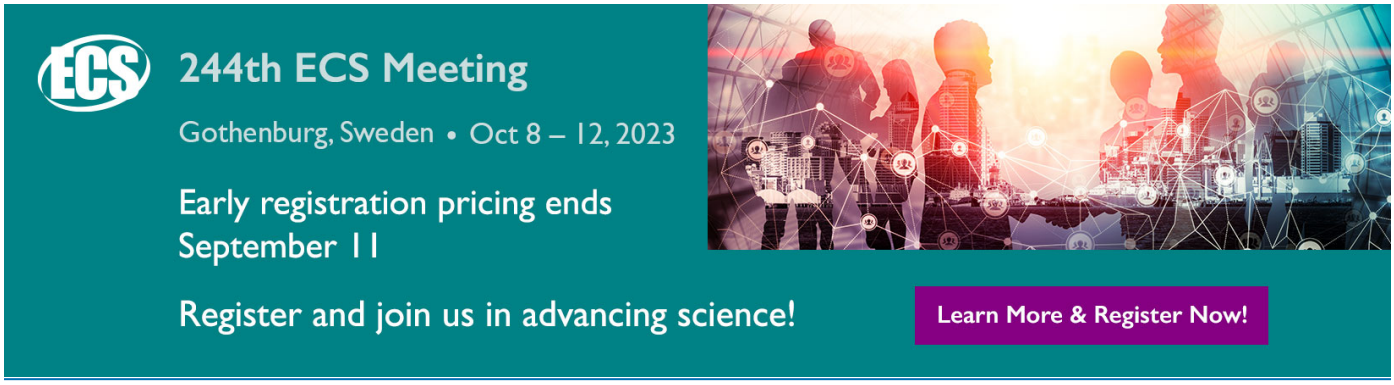

Journal of The Electrochemical Society, 2023 **170** 080503

Ageing of High Energy Density Automotive Li-Ion Batteries: The Effect of Temperature and State-of-Charge

Anastasiia Mikheenkova,[1,z] Alexander J. Smith,[2] Kristian B. Frenander,[3] Yonas Tesfamhret,[1] Niladri Roy Chowdhury,[4] Cheuk-Wai Tai,[5] Torbjörn Thiringer,[3] Rakel Wreland Lindström,[2] Maria Hahlin,[1,6] and Matthew J. Lacey[7]

[1]*Ångström Laboratory, Department of Chemistry, Uppsala University, SE-751 21 Uppsala, Sweden*
[2]*Applied Electrochemistry, Department of Chemical Engineering, KTH Royal Institute of Technology, SE-100 44 Stockholm, Sweden*
[3]*Department of Electrical Engineering, Chalmers University of Technology, 412 96 Gothenburg, Sweden*
[4]*Volvo Group Trucks Technology (GTT), 405 08 Gothenburg, Sweden*
[5]*Department of Materials and Environmental Chemistry, Arrhenius Laboratory, Stockholm University, Stockholm, 10691 Sweden*
[6]*Ångström Laboratory, Department of Physics and Astronomy, Uppsala University, SE-751 21 Uppsala, Sweden*
[7]*Scania CV AB, Södertälje, 151 87, Sweden*

Lithium ion batteries (LIB) have become a cornerstone of the shift to electric transportation. In an attempt to decrease the production load and prolong battery life, understanding different degradation mechanisms in state-of-the-art LIBs is essential. Here, we analyze how operational temperature and state-of-charge (SoC) range in cycling influence the ageing of automotive grade 21700 batteries, extracted from a Tesla 3 long Range 2018 battery pack with positive electrode containing $LiNi_xCo_yAl_zO_2$ (NCA) and negative electrode containing SiO_x-C. In the given study we use a combination of electrochemical and material analysis to understand degradation sources in the cell. Herein we show that loss of lithium inventory is the main degradation mode in the cells, with loss of material on the negative electrode as there is a significant contributor when cycled in the low SoC range. Degradation of NCA dominates at elevated temperatures with combination of cycling to high SoC (beyond 50%).
 [DOI: 10.1149/1945-7111/aceb8f]

Manuscript submitted April 25, 2023; revised manuscript received June 22, 2023. Published August 8, 2023.

Supplementary material for this article is available online

The future of passenger road transport is electric. The phase-out of fossil fuel vehicles is now closer than ever, with targets such as the "Fit for 55" package within the European Green Deal aiming to ban petrol- and diesel-powered cars and vans from the European Union market by 2035.[1–4] Lithium-ion batteries (LIB) are widely considered to be the key technology enabling electrification.[5] Solutions for prolonging battery life are motivated by reasons of economics and sustainability, particularly concerning the high energy demand of production and the scarcity of key materials.[6–8] A significant focus in degradation studies of electric vehicle (EV) grade batteries is placed on cycling conditions. Finding an optimal combination of cut-off potential together with cycling temperature can significantly prolong battery life.[9]

In this study, we focus on the ageing and degradation of a Tesla 21700 cylindrical cell, which is composed of a blended graphite-SiO_x composite negative electrode and an NCA ($LiNi_xCo_yAl_zO_2$) positive electrode, both currently considered state-of-the-art in EV cells. Among the most widespread chemistries used for the positive electrode in LIBs (NCA, NMC, LFP, and LMO) NCA shows the higher gravimetric capacity and specific energy.[10] A number of comprehensive studies are performed on the NCA and analogous materials as well as on its operation in commercial cells.[9,11–16] The results have demonstrated that the state of charge (SoC) range has a significant influence on the ageing of the cells. The choice of the appropriate SoC range as well as the cycling temperature can significantly improve the cell battery life. The majority of research on battery systems is, however, conducted on model systems in the laboratory and typically with a focus on the positive electrode. Nonetheless, automotive-grade cells are much more optimized which, as well as the larger form factor, can influence the degradation processes. A forthcoming study done in parallel reveals the SoC dependence of the ageing processes in these particular cells by cycling in narrow ranges (Δ10% SoC).[17] In the current study, we extend the work to conditions more relevant to long-haul vehicle use, including broader cycling windows and higher temperature. We thereby focus on the combined effects of temperature and SoC range through full cell electrochemical evaluation and post mortem analysis of harvested electrodes from automotive-grade batteries.

Battery ageing studies are complex due to the interrelation of multiscale processes, requiring multiple techniques for a profound analysis and often interpretations can be often challenging due to technical limitations.[18] Most of the ageing studies are focused on cell, electrode, or material levels[19] and the challenge to distinguish individual ageing processes has motivated the classification of ageing mechanisms into three major ageing modes: loss of lithium inventory (LLI), loss of active material (LAM), and loss of electric conductivity also known as resistance increase (RI).[20–24] LLI refers to processes that result in a loss of lithium ions available to participate in the redox process, such as the formation of the solid-electrolyte interphase (SEI), while LAM covers processes that involve loss or changes resulting in the lower electrochemical activity of the host material, including transition metal dissolution, irreversible phase transition, and particle disconnection as a result of particle cracking. RI is related to the degradation of current collectors and binder. LLI and LAM modes are shown to be dominant.[24,25] Notwithstanding its practical utility, it is important to acknowledge that the degradations modes represent a simplified approach for evaluation of battery ageing. In most cases, degradation mechanisms influence more than one mode (i.e. SEI formation is a classic example of LLI degradation mode, yet it will introduce RI as well; disconnection of SiO_x is LAM, however, it will also include LLI if the particle got disconnected when Li is inside the particles, etc.).

The degree of ageing of a cell is often reported as its state of health (SoH), which is calculated as the ratio of an observed capacity

[z]E-mail: anastasiia.mikheenkova@kemi.uu.se

to the initial or nominal capacity of the cell.[26] To understand the sources of capacity loss and resistance increase, various electrochemical characterization techniques are used, including incremental capacity analysis (ICA) and differential voltage analysis (DVA).[27] ICA and DVA provide information about the close-to-equilibrium state of the cell. Both of the analyses may be supported with techniques that analyze electrochemical dynamics, e.g. electrochemical impedance spectroscopy (EIS) and current interruption techniques. Together these give insights into general ageing trends in the battery as well as possible sources of capacity loss and internal resistance growth. Such analysis is feasible for commercial cells, yet, the possibility of testing the electrodes in three-electrode cell setup or half-cells allows the deconvolution of separate resistance contributions.[28] For the inactive components, binder decomposition, conductive additive oxidation, and current collector corrosion are highlighted as ageing causes.[29] The anode active material ageing is mainly caused by SEI instability, lithium plating, and the loss of electrical contact in the active material.[30,31] As for the positive electrode, generally, micro-cracking of secondary particles, structural disordering, phase transitions to inactive phases, transition metal dissolution, and reactions with the electrolyte are listed.[32,33] However, the extent of each mechanism is specific to the choice of active materials. Especially, for Ni-rich materials these are shown to be dependent on the Ni content and type of doping.[32,34,35] The extent to which different degradation mechanisms contribute to the overall ageing depends on the cycling conditions. For example, particle cracking of Ni-rich active material is prevalent at a high state of charge (SoC),[36] and degradation sensitivity towards temperatures has been previously shown.[11,37] Other detrimental processes can be accelerated with elevated temperatures, such as SEI thickening and dissolution.[38]

The development of LIBs has been the subject of extensive research in both academic and industrial settings. However, there is still a gap between the results obtained from model systems and the actual batteries in use.[39] In order to address this issue, this study uses a combination of electrochemical and material studies to investigate ageing in state-of-the-art batteries and address the relevance of current ageing theories. The study aims to leverage access and skill in a large network to do an in-depth study of ageing processes in a commercially relevant cell. Specifically, the cells were subjected to ageing tests at three different state-of-charge (SoC) ranges (0%–50% SoC, 50%–100% SoC, and full SoC) and two cycling temperatures (22 °C and 45 °C) to identify the dominant agents of ageing.

Experimental

Materials.—Laminated aluminum pouch material (Skultuna Flexible), 1-Methyl-2-pyrrolidone (NMP, 99.5%, anhydrous, Sigma-Aldrich), 1 mol l^{-1} lithium hexafluorophosphate dissolved in 1:1 v/v ethylene carbonate:diethyl carbonate (LP40, 1 M LiPF6 in 1:1 EC:DEC, Solvionic), lithium metal chips (Li, MTI Corporation, thickness 450 μm, ∅1.55 cm, 90 mAh cm^{-2}), quartz capillaries (∅5 mm, wall thickness 0.01 mm, Hilgenberg), and glass fiber separators (Whatman® GF/A) were used as received. Trilayer Microporous Membrane (PP/PE/PP) separators (Celgard 2325, 25 μm) were cleaned with ethanol and deionized water and dried under vacuum at 60 °C for 12 h in the glovebox).

Commercial cells cycling ageing.—The 21700 cells were extracted from a battery pack of a relatively new Tesla 3 long Range from the year 2018. The unaged cells are further referred further to as the Beginning of Life (BoL). Naturally, the cells underwent the process of formation. After this, the vehicle went through an undefined low number of cycles before it was dismantled. Therefore, in this manuscript, we define the BoL in relation to the tests that the cell was subjected to. The cells were cycled within 0%–50%, 50%–100% and 0%–100% SoC ranges at constant temperatures: at 22 °C and 45 °C correspondingly using a NEWARE BTS-4000 battery tester within a constant temperature test chamber. Duplicate cells were cycled under each condition. The SoC levels during cycling were defined via voltage limits (Table I). In order to account for polarization during cycling the voltage limit corresponding to 50% SoC is different depending on whether it is a charge or discharge to 50% SoC. The cycling test matrix and naming of the cells are based on cycling conditions and are listed in Table I (for more details see Supporting Information (SI) Table SI) where R denotes room temperature (22 °C), H denotes high temperature (45 °C) and numbers following the letter indicate cycling intervals during ageing in terms of % SoC. C/3 (1.53 A) and 1C (4.6 A) current rates were used as charging and discharging current respectively. After each 50 Full Cycle Equivalents (FCE) a reference performance test (RPT) was conducted. During each RPT, one cycle at C/3 charge and discharge rate was performed to initialize cells for RPT and ensure uniform test conditions throughout the RPT. Then two cycles with a CC–CV charge with C/20 cut-off at maximum voltage and C/3 discharge to minimum voltage was performed to measure capacity. An average of the two discharge capacity measurements is used as a capacity value for that RPT. Furthermore, a C/20 full cycle is performed for incremental capacity analysis purposes, which is followed by discharge and charge pulses at the cycler maximum current of 1.3C at 30%, 50% and 70% SOC levels to track impedance. A visual clarification of the RPT is included in SI Fig. S1. The cells were stopped when reaching ∼75% SoH, unless they had to be stopped earlier due to the time limitations of the project (an example of such is a cell cycled between 50%–100% SoC at 22 °C).

State of Health (SoH) is defined as a capacity retention as measured during a C/3 discharge related to the initial capacity and expressed in percentage of initial capacity. State of Charge was set by fixed voltage levels to avoid drifting in SoC window during cycling. The voltage limits were set based on reference tests with relevant C rate (i.e., 1C for voltage during discharge and C/3 for charge procedure, for the partial SOC window tests). For R0–100 and H0–100 cycling was performed between maximum and minimum voltage of the cell. The raw data of reference performance tests is available on Zenodo depository.[40]

Cell tear down.—All cells were discharged to 0% SoC (∼2.55 V) before disassembly and opened in a dry, Ar-filled glovebox. For each cell, electrodes were carefully unrolled and cut in segments of equal size, respecting the orientation of the electrodes to one another as well as to the cell terminals. Segments were numbered Region 1 to 6 where 1 is the closest to the cell casing and 6 is the closest to the core. Region 4 was located ∼400 mm from the beginning of the positive electrode and 480 mm from the beginning of the negative

Table I. Sample matrix.

Sample name	SoC range	Upper voltage	Lower voltage	Temperature
R0–50	0%–50%SoC	3.78 V	2.55 V	22 °C
R50–100	50%–100% SoC	4.18 V	3.53 V	22 °C
R0–100	0%–100% SoC	4.18 V	2.55 V	22 °C
H0–50	0%–50%SoC	3.78 V	2.55 V	45 °C
H50–100	50%–100% SoC	4.18 V	3.53 V	45 °C
H0–100	0%–100% SoC	4.18 V	2.55 V	45 °C

electrode and considered central. Additionally, Region 4, was split into three equal parts within the height called U, C, and D, where U is the closest to the negative terminal, C is in the center and D is close to the positive terminal. The heterogeneity of ageing within the cell was evaluated by selecting samples at three different positions in the height direction from the center of Region 4. The electrodes collected within the height of the cell U, C, and D were taken from ~15, 32, and 47 mm from the top of the cell (the scheme of the electrode regions is shown in "Degradation inhomogeneity" section). Afterwards, the segments were stored in individual pre-dried plastic bags and sealed in pouch bags. Electrodes were harvested at BoL from an unaged cell and at end of life (EoL) from cycled cells from each of the six test groups.

Electrochemical measurements of extracted electrodes.—A Biologic MPG2 was used for post-disassembly electrochemical testing. One side of the active material coating on the extracted electrodes was removed using a scalpel after pre-soaking in NMP for the positive electrode and methanol for the negative electrode. The absence of samples preparation artifacts (such as electrode delamination) was confirmed using cross section image obtained with scanning electron microscope (the technical details of the sample preparation and scanning microscope analysis are presented further). The positive electrodes were punched ∅10 mm and the negative electrode using an ∅11 mm puncher. The pouch cells were assembled with electrolyte LP40, Celgard 2325 separator in a half-cell configuration. A part of the cells from Region 4 was tested using a gold micro-reference electrode as a reference electrode to measure lithium diffusion resistance coefficient without the contribution of the counter electrode (Li).[41] The cells were cycled at room temperature between 2.55 and 4.2 V for the positive and between 1.5 V and 0.05 V for the negative electrode with a constant current of C/10 (275 μA) after a 4 h rest. A combination of constant current cycling and intermittent current interruption (ICI) was performed to evaluate the electrode performance. ICI was carried out by introducing a 5s rest every 5 min.[42] During the current interruptions, the voltage was recorded with time resolution of 0.05 s. The ICI data were treated using the script developed by Lacey et al.[43] To compare cells cycled at different conditions, the lithium diffusion coefficient k was averaged for the plateau region between 2 to 3 mAh cm^{-1}. More details on ICI method can be found in supporting information, section "Intermittent current interruption."

Additional two-electrode, vacuum-sealed pouch cells were built and tested in the interests of evaluating lab-to-lab reproducibility (Uppsala University and KTH Royal Institute of Technology) and generating robust metrics of electrode capacity. These cells contained NCA or Gr-SiO$_x$ electrodes harvested from the cylindrical cells, lithium foil (Sigma-Aldrich) as a counter/reference electrode, Whatman® GF/A separator, and the same electrolyte. At KTH, cycling was done at an estimated 0.1C rate (NCA: 0.40 mA cm^{-2}, Gr-SiOx: 0.45 mA cm^{-2}) on an in-house, high-precision battery cycler using Keithley 220 programmable power sources. Cycling of the NCA cells was occasionally conducted with higher cutoff voltages of up to 4.35 V vs Li/Li$^+$. In the cases with higher cutoff voltages, the discharge and differential voltage profiles are translated to match the initial discharge voltage of the corresponding three-electrode cell. The discharge curves are shown in SI Figs. S2 and S3 (positive and negative electrodes correspondingly).

Test cell data already processed for ICI did not require additional smoothing for DVA. The other test cell data were smoothed using the strategy first suggested by Li et al.[44] and applied in our earlier work,[45] with an initial moving average smoothing step over a 0.55% SoC span and a Gaussian filter over a 3.0% SoC span. The differential voltage parameter was obtained by numerical differentiation of the discharge curves (corresponding to the second complete discharge of each half-cell) and normalization by the discharge capacity (DV = Q_d·dV/dQ). Peaks were identified manually using ipf.m, Interactive Peak Fitter.[46] All smoothing, peak identification, and differential voltage analyses were performed in MATLAB®.

The raw data of half-cell tests is available on Zenodo depository.[40]

Scanning electron microscopy and energy-dispersive X-ray spectroscopy studies.—A Zeiss LEO 1530 with an Oxford AZtec EDS system was used to perform scanning electron microscopy (SEM) and energy-dispersive X-ray spectroscopy (EDS). SEM with InLens detector was performed using an acceleration voltage of 5 kV and a working distance of 6.5 mm for cross-section images and 5.0 mm for top-view images. Elemental distribution within the positive and negative electrodes was also measured with EDS using acceleration voltage 20 kV and distance 8.5 mm. Cross section sample preparation of electrodes were done using ion polishing. The methodology is further described in our previous study.[47]

Inductively coupled plasma - optical emission spectrometry.—An Avio 500 Scott/Cross-Flow Configuration was used for elementary composition identification using inductively coupled plasma - optical emission spectrometry (ICP-OES). Disks of positive and negative electrodes were punched from each cell: room and 45 °C ageing within 0%–50%, 50%–100%, and 0%–100% SoC. Region 4 from positive and negative electrodes of each sample was used for comparison. One disk ∅10 mm for positive electrode and two disks ∅20 mm for negative electrode were used per sample. The followed detailed methodology for further sample preparation can be accessed in our previous study.[47]

X-ray diffraction.—The extracted powder from the electrode in Region 4 in each cell was ground by hand in a mortar and pestle and sealed in quartz capillary in a dry, Ar filled glovebox using an epoxy glue. For the X-ray diffraction (XRD) data collection a STOE Stadi P diffractometer with Ge source and a Dectris Mythen 3 K detector was used. The data was collected utilizing Cu Kα radiation (λ = 1.5406 Å) in Debye–Scherrer mode and fitted using commercially available software TOPAS V6.[48]

Transmission electron microscopy.—TEM lamellae of BoL and EoL samples were prepared using a Focused Ion Beam (FIB) on model Crossbeam 550 (Zeiss). The surface of the sample was masked with a carbon and a Pt layer. A 2 kV ion accelerating voltage was used for sample polishing. The lamellae were studied with scanning transmission electron microscopy (STEM) using a double aberration-corrected Themis Z (Thermo Fisher). The microscope was operated at 300 kV and equipped with a Super-X EDS detector. The aberrations in the condenser lens system were corrected up to 5th order. The collection angle for HAADF- and BF-STEM imaging were 63–200 mrad and below 35 mrad, respectively. Imaging and EDS acquisition and analyses were performed using Thermo Fisher Velox.

Results

Cell composition.—In the opened 21700 cylindrical cells the positive electrode was measured to be 920 × 64 mm (both sides); the negative electrode was measured to be 65 mm height, with a coating length of 855 mm on the convex side of the coating and 920 mm on the concave side. The negative current collector measured 940 mm and had a clean copper part facing the cell casing. The separator oversized by 1 mm at the top and bottom of the negative electrode. The 21700 cells in the Tesla 3 long Range 2018 battery pack had similar chemistries of the positive and negative electrodes reported for Tesla Model S 18650 cells[37] and Panasonic cells.[10,13,49] SEM/EDS analysis revealed that the positive electrode was composed of NCA, carbon conductive additive, and a polymer binder. The active material consisted of secondary particles of $Li_xNi_{0.90}Co_{0.05}Al_{0.05}O_2$ doped with ~1% W (confirmed with ICP and EDS SI Fig. S11) and primary particles in a range of ~100 nm. W doping of NCA is

known to increase electronic and ionic conductivity, decrease cation mixing, and mitigate particle cracking.[50] The negative electrode consisted of graphite with SiO_x particles, which had a coating or interphase layer with a thickness up to 100 nm. The use of SiO_x chemistry in the negative electrode has been found to improve its specific capacity and lower degradation compared to pure Si.[51]

SEM images of cross-sections of the electrodes showed that the positive electrode was double-coated with an Al foil with a thickness of 15 μm and a coating thickness of ~65 μm (Fig. 1a). The active material loading was measured at ~22.9 mg cm^{-2}. The negative electrode consisted of a copper foil with a thickness of 8 μm with a double-sided coating of ~85 μm and a loading of ~11.7 mg cm^{-2} (Fig. 1b). The separator extracted from the cell had a morphological similarity to polypropylene (PP)/polyethylene (PE) separators (SI Fig. S5) and a coating on the side towards the positive electrode that was based on Al_2O_3 or $Al(OH)_3$ (probed with EDS), which are often used to improve thermal properties, puncture strength, and limit cross-talk between the cathode and anode.[52–54]

Full cell degradation analysis.—The present study investigates the long-term cycling performance of cells under different operational conditions, as shown in Table I. Capacity loss was evaluated in the change in SoH with increasing number of FCE where one FCE measured based on the cell initial capacity (Fig. 2a).

$$N_{FCE} = \frac{Total\ discharge\ throughput}{Nominal\ capacity}$$

The observations of the capacity loss trends enable a comparative evaluation of cell performance under varied conditions. In the studied case, the capacity loss curve indicates a sublinear ageing trajectory, as the cells did not reach the knee point where degradation is expected to accelerate.[55] The last point of each dataset corresponds to the last measurement of remaining practical capacity before the cell was disconnected. The difference in end-of-life (EoL) capacity between cells will be taken into consideration for every trend analysis.

The capacity retention above 95% is similar for all ageing conditions, except for the cells cycled at 50%–100% SoC at 22 °C (R50–100), which exhibit better capacity retention. Even so, the cells in this work all degrade faster (in terms of FCE) than their counterparts cycled in narrow windows (Δ10% SoC) in our parallel, forthcoming study. This may be attributable to the development of larger stresses and heterogeneity in cells cycled over a broader SoC range. Cells cycled between 0%–50% and 0%–100% SoC (R0–50, H0–50, R0–100, and H0–100) at both temperatures show a similar trend of capacity fading down to 85% SoC, as depicted in Fig. 2b. The cells cycled at 50%–100% SoC at both 22 °C and 45 °C exhibit a slower decay and longer lifetime compared to the other cells in this work. Among these, the cells cycled at 22 °C demonstrate superior performance compared to those cycled at 45 °C. Furthermore, the cells cycled between 0%–100% SoC at 22 °C (R0–100) degrade quicker than the others.

In order to compare the rates of cell ageing, the number of FCE required for each cell to reach ~80% SoH are determined. For most conditions, the cycle life is around 600–700 FCE. However, the cells aged within the 50%–100% state of charge (SoC) range have a significantly higher number of FCE compared to the rest of the cells. The H50–100 cell has undergone approximately twice as many cycles (~1200), while the R50–100 cell has undergone more than three times as many cycles (~2400). This suggests that cells cycled at high SoC (50%–100%) at both room (22 °C) and high (45 °C) temperatures outperformed the other cells by a factor of 2 and 4 respectively.

The electrochemical behavior of cells was visualized using incremental capacity analysis (ICA). ICA profiles at BoL, an intermediate cycle number or Middle of Life (MoL, 300 FCE), and EoL (~75% capacity retention) are depicted in Fig. 3, illustrating the evolution of electrochemical behavior. MoL was defined as half number of FCE before cell reached 80% capacity retention for the cells that have degraded most rapidly. The peaks identified in the fresh cell are attributed to regions of reaction stability in both electrodes and are labeled accordingly (Fig. 3a). During charging, NCA undergoes multiple phase transitions, including the transitions from hexagonal H1 to monoclinic M (reaction ④), intermediate monoclinic behavior (reaction ③), monoclinic M to hexagonal H2 (reaction ②), and hexagonal H2 to hexagonal H3 (reaction ①).[56,57] Lumped silicon oxide behavior is represented by reaction ❹. Graphite (de)lithiation occurs through several well-ordered stages, with several lumped dilute stages exchanging until stage III (LiC_{27}, reaction ❸), stage III exchanging with stage II (LiC_{12}, reaction ❷), and stage II exchanging with stage I (LiC_6, reaction ❶).[51,58,59] The peak ④ × ❹ is used to track the changes in the silicon oxide fraction of the blended negative electrode. All other ICA features arise due to convolutions of NCA and graphite (de) lithiation reactions. The evolution of these features supports qualitative discussion of the observed ageing behavior.

In general, it is noted that as the cells age, the peaks become wider and less distinct. This can indicate the effects of lithiation heterogeneity within the electrodes. This uneven distribution of lithium can arise due to slowed reaction or diffusion kinetics and other localized ageing processes.[20,60,61] Heterogeneity causes peaks

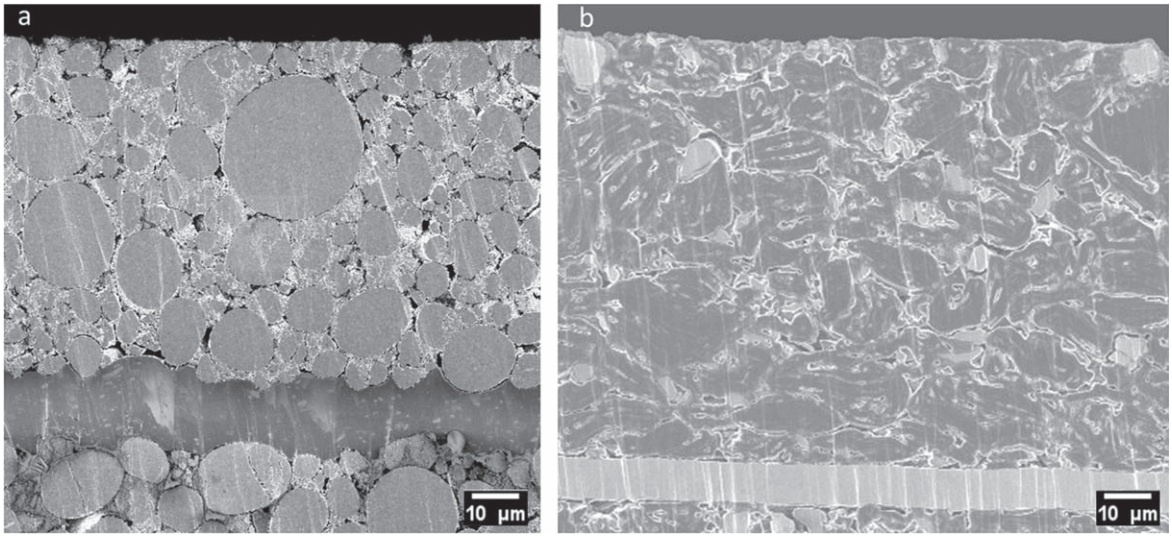

Figure 1. SEM images of the cross-section of (a) positive and (b) negative electrodes.

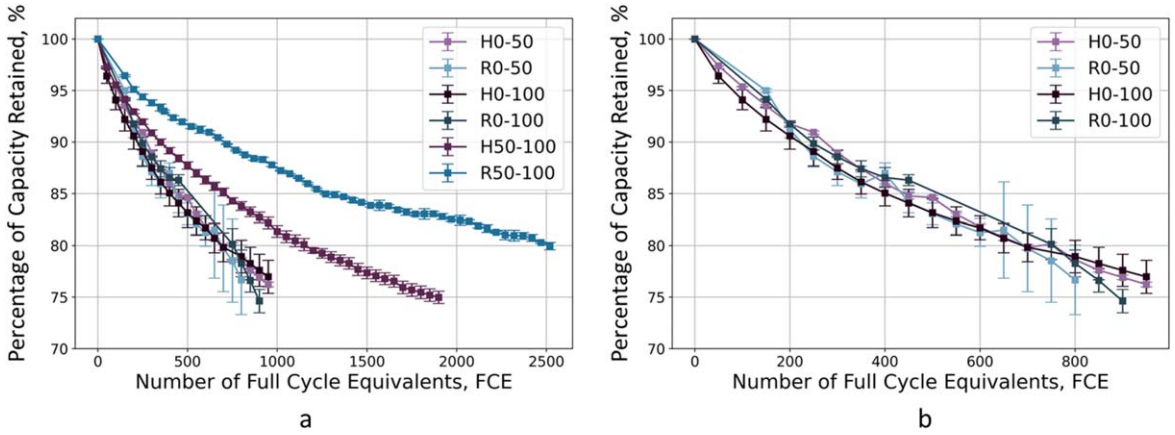

Figure 2. Percentage of capacity retention of 21700 Li-ion cells at different cycling conditions: all cells (a), zoomed view to show the similarity among cells cycled between 0–50 and 0%–100% SoC at 22 °C and 45 °C are shown separately from high SoC cells for better resolution (b).

to blend into one another, since it causes local differences in capacity within the cell and thus shifts the local electrode potentials. The reactions then occur, still sequentially in each particle, but over a distribution of times during charge/discharge and at different points of overall cell voltage. Heterogeneous ageing is also confirmed by local capacity measurements during post mortem analysis, see section "Degradation inhomogeneity." This trend is consistent across all cycling conditions and shows no clear dependence on temperature nor SoC window, with all EoL ICA profiles showing fewer distinct peaks. In particular, peaks ③ × ❸ and ③ × ❷, which are inherently less pronounced already at BoL, cannot be resolved visually in ICA after extended cycling. This likely represents increases in both resistance and heterogeneity in all cells.

For the R50–100 and H50–100 cases, shown in Figs. 3d and 3e respectively, a shift of all peaks towards higher full cell voltage is visible. This is attributed to loss of lithium inventory (LLI),[51] by which electrode slippage shifts the operating windows of the electrodes to higher potentials.

In the cases where the cells were fully discharged during cycling, Figs. 3b, 3c, 3f, and 3g, all show that peak ④ × ❹ is lost, or greatly diminished, already after 300 FCE compared to H50–100 and R50–100 cells which clearly show the ④ × ❹ peak. As the graphite peak are still clearly visible, this indicates uneven ageing in the blended electrode with a rapid loss of active silicon oxide when discharging to (and charging from) 0% SOC. Our parallel work suggests that the upper limit of this damaging effect is around 25% SoC.[17] For H50–100, this characteristic peak (④ × ❹) is preserved, albeit shifted, during cycling, indicating retained activity of the silicon oxide fraction of the electrode. It is noted that the loss of this peak ④ × ❹ in the R50–100 case, shown in Fig. 3d, shows that active silicon may also be lost during cycling in a higher SOC window. However, higher resistance and local heterogeneity might also to some extent contribute to apparent losses of this weakly-prominent peak.

The shift in the trough between peaks ② × ❶ and ② × ❷ to higher voltages is an indicator for LLI.[45] However, this might only be possible to capture by tracking intermediate stages (see MoL profiles in Fig. 3) and the observation that the trough deepens between NCA reactions ① and ②. That becomes coincident with the trough between graphite reactions ❶ and ❷ (Fig. 3e). In cases of increasing heterogeneity, the distinction between ② × ❶ and ② × ❷ may simply smear out to form one broad peak representing both concurrent equilibria. The gradual loss of peak height in ① × ❶ seen in all ageing cases is a better indicator of LLI for cells containing NCA and graphite. For this to be true, the ① × ❶ peak must remain prominent and separated from the other smeared peaks (so that the decrease is not due solely to lithiation heterogeneity). In such cases, less of the fully-lithiated LiC_6 phase can be formed on charge once lithium is consumed at the negative electrode. Although selective LAM presents in some ageing cases and increasing heterogeneity is observed throughout, the changes in peak ① × ❶ for all samples indicate that LLI always occurs to a significant extent.

Post mortem analysis.— *Degradation inhomogeneity.*—The ICA of the full cell cycling data has indicated ageing heterogeneity within the cell. To address spatial heterogeneity, corresponding positive and negative electrodes from the cell roll were tested. The evaluation of heterogeneity was done to anticipate its effect for the following ex situ tests. Local half-cell capacity was addressed for the positive and negative electrodes respectively in several different regions, where Region 1 corresponds to the cell casing and Region 6 is the cell core (Fig. 4, electrodes are shown not to scale). H0–100 cell was used for the evaluation as it experienced the most severe positive electrode degradation. For the positive electrodes the H0–100 aged cell showed the most severe degradation in the central region. The least aged region (highest capacity retention) is the Region 6, located in in the core of the cell, while the Region 1, which is closest to the cell casing, showed comparable degradation with the central region. The highest capacity loss of the negative electrode in the middle height of the cell was found in Region 1 (closer to the cell casing). The heterogeneity in ageing within the electrode roll was also done at various heights for the central Region 4 of the cell. For consistent comparison among cells the electrodes were cut at the same distance from the top of the cell. The most severe ageing for the positive electrode was detected for the middle height of the cell. This is consistent with previous studies that evaluate the capacity loss distribution within cylindrical cells.[37,62] The negative electrode shows the opposite trend and the lowest capacity was found towards the bottom of the cell. For further consistent comparison in post mortem studies among cells, the centre of Region 4 was chosen and the electrodes were cut at the same distance from the top of the cell.

Electrochemical analysis of capacity loss in the positive and negative electrodes.—Upon reaching end-of-life (EoL), the cells were disassembled and the positive and negative electrodes from the center (Region 4) were evaluated in a half-cell configuration. Figure 5 presents the capacity loss of the positive and negative electrodes from aged cell expressed as a percentage of the cell capacity at BoL. The capacity loss depicted in Fig. 5 reveals that for the cells cycled at both temperatures between 0%–50% State of Charge (SoC), the negative electrode exhibits higher capacity loss. Also, all cells cycled at 22 °C demonstrated a dominant capacity loss in the negative electrode. On the contrary, the cells cycled at 45 °C 50–100 and 0%–100% SoC exhibited a relatively greater capacity loss of the positive electrode, compared to their 22 °C counterpart. The positive electrode operating between 0%–50% SoC at 22 °C (R0–50) demonstrated the lowest capacity loss. These observed trends are consistent with what is commonly observed for nickel-rich

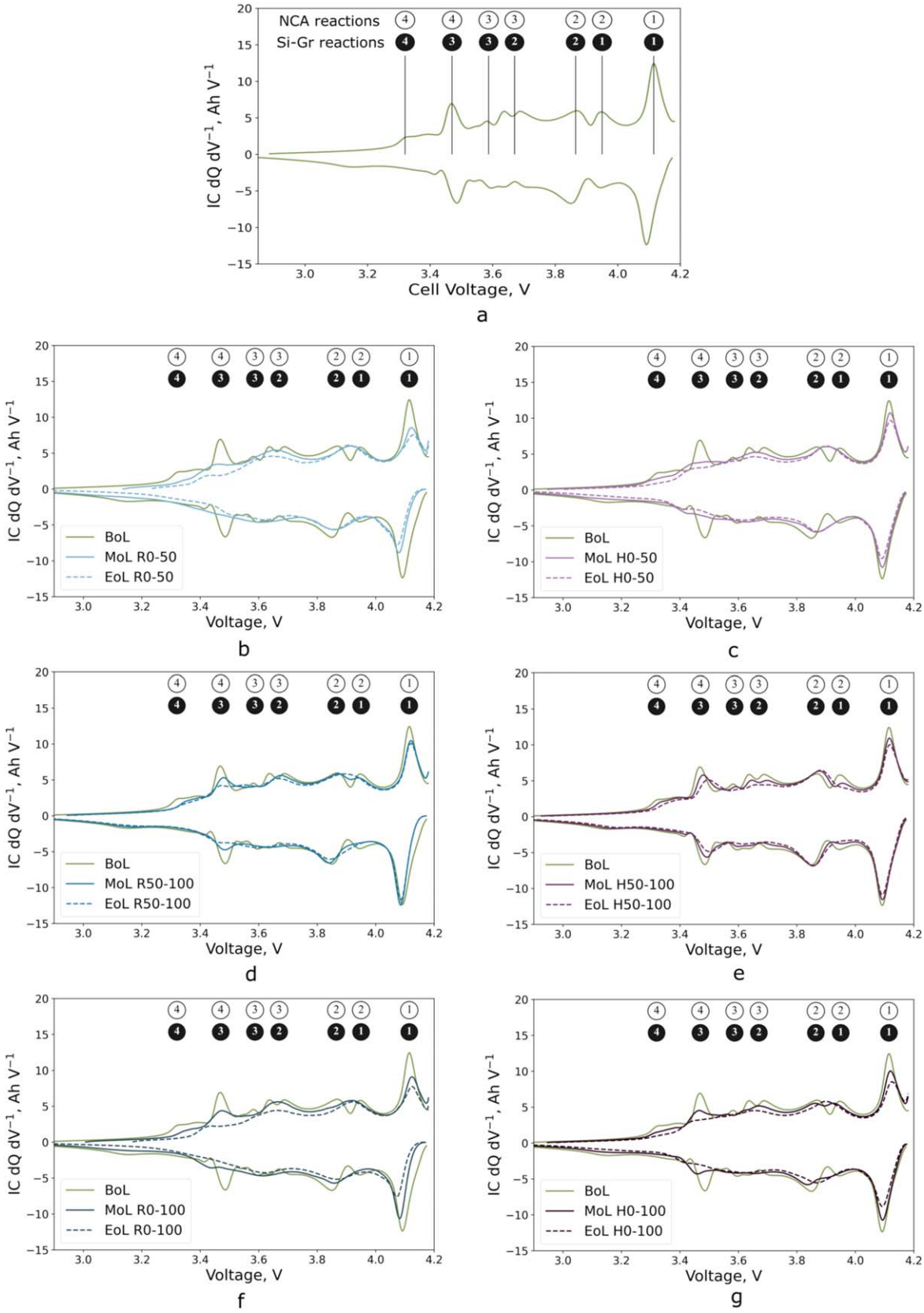

Figure 3. ICA comparison of cells at BoL (0 FCE), MoL (300 FCE), and EoL aged under various conditions: BoL cell with reactions specified (a); R0–50 cell cycled between 0%–50% SoC at 22 °C (b), H0–50 cell cycled between 0%–50% SoC at 22 °C (c), R50–100 cell cycled between 50%–100% SoC at 22 °C (d), H50–100 cell cycled between 50%–100% SoC at 22 °C (e), R0–100 cell cycled between 0%–100% SoC at 22 °C (f), H0–100 cell cycled between 0%–100% SoC at 22 °C (g).

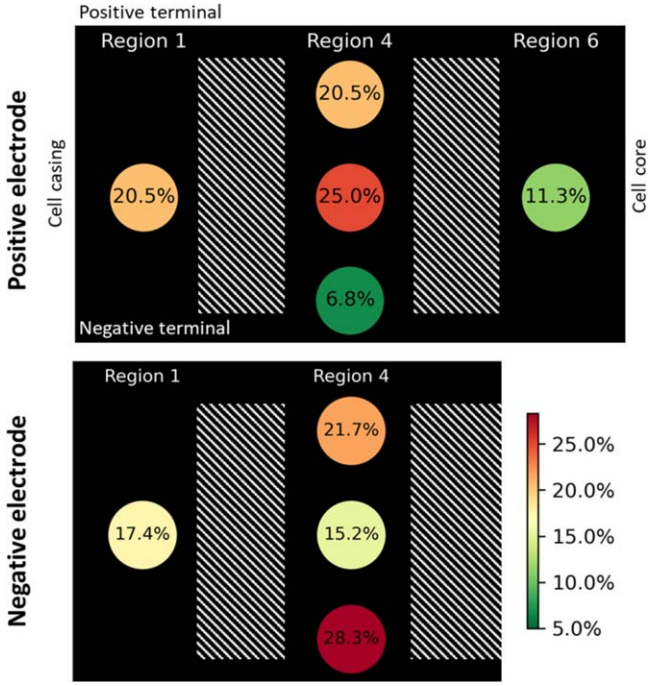

Figure 4. Capacity loss distribution in the positive and negative electrodes of an H0–100 cell.

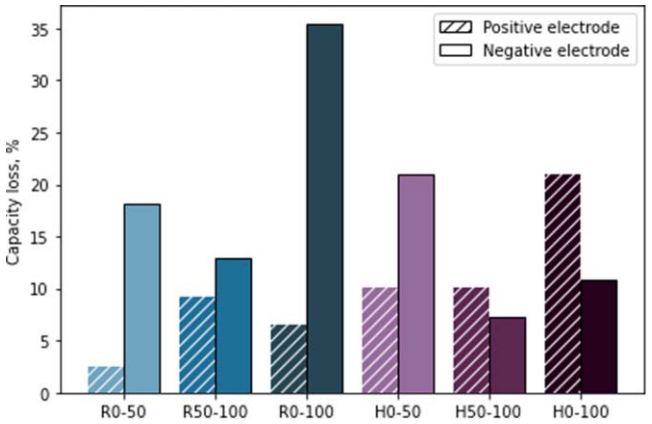

Figure 5. Capacity loss evaluation of positive and negative electrodes harvested from the center of the jellyroll (Region 4) of aged cells as a percentage of BoL capacity.

electrodes, as the majority of the degradation processes are linked to material delithiation beyond 75% of lithium content in the cathode material.[22] The results demonstrate that cycling at elevated temperature accelerates the degradation of the NCA-electrode, whereas the low SoC window (0%–50%) is more detrimental for the SiO_x-Gr electrode.

The difference in used cyclable capacity window (Q_{window}) and LLI reflected in mAh cm^{-2} in a full cell configuration is presented in Fig. 6. Q_{window} is a term used to demonstrate the capacity which can be utilized in the cells in full cell configuration and is defined here as difference between charge endpoint of the positive electrode ($Q_{PE\ Ch}$) and discharge endpoint of the negative electrode ($Q_{NE\ D-ch}$).

$$Q_{window} = Q_{PE\ Ch} - Q_{NE\ D-ch}$$

A decrease in the Q_{window} is generally coming from capacity loss and a change in positive vs negative electrodes capacity balancing.[63] The detailed analysis methodology for used capacity is presented by Birkl et al.[21] In this study, the loss of cyclable capacity window is

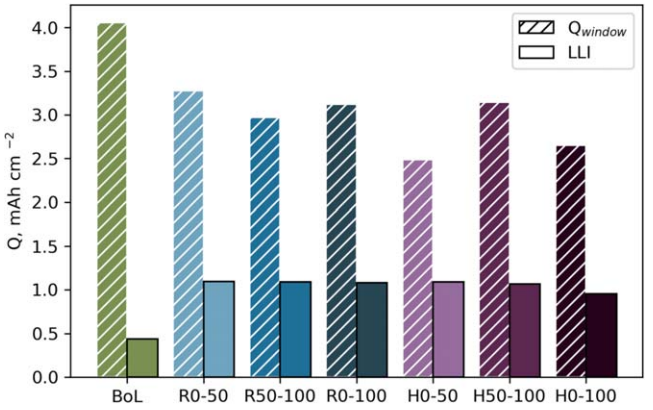

Figure 6. Comparison of a cyclable capacity window and LLI for the studied cells.

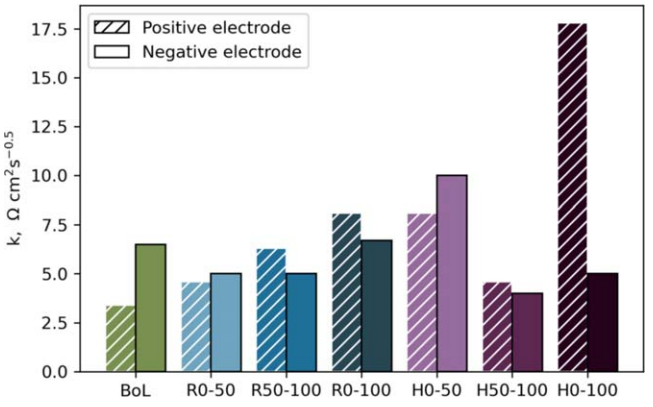

Figure 7. Comparison of Li diffusion resistance coefficient of cells aged within 0%–50%, 50%–100%, and 0%–100% SoC at 22 °C and 45 °C for positive and negative electrodes.

found to be similar for cells cycled at 22 °C (all SoC window) and cell cycled 50%–100% SoC at 45 °C. Additionally, the LLI was analyzed for all aged cells and showed that LLI is responsible for most of the capacity loss in the studied cells. Interestingly, LLI values are very close for all condition with a slight deviation except for the cell cycled at 45 °C between 0%–100% SoC. LLI is often suggested as one of the main degradation mechanisms in LIB.[25] The observed LLI and its extend supports the trends observed with ICA presented in Fig. 3.

Intermittent current interruption (ICI) cycling protocols and analysis reveal solid state Li^+ diffusion resistance coefficients, k.[64,65] Changes of k can be due to an alteration of the effective diffusion length (for example, particle cracking or increased tortuosity), the formation of surface layers such as rocksalt, which introduce lattice mismatch along the diffusion path of Li^+, or other structural changes in the active material.[66,67] Figure 7 shows a comparison of the Li^+ diffusion resistance coefficients of the extracted aged electrodes. For the aged positive electrodes, k increased most significantly for the H0–100 cell (~6 times). For other conditions such as R50–100, R0–100, and H0–50, the increase in k is approximately 2 times compared to the BoL. As for the negative electrode, room temperature ageing did not increase k, but rather imposed a slight decrease. The high-temperature cycling led to a decrease for the H50–100 and H0–100 aged cells, and a ~1.5 times increase in k for the H0–50 aged cell. The decrease of k on the negative electrodes might be influenced by an increase of graphite interlattice spacing during ageing.[68]

Detailed analysis of the degradation of the NCA positive electrode.—In order to evaluate loss of active material on the

positive electrode (LAM_{PE}), a differential voltage analysis (DVA) was conducted and the results are presented in Fig. 8. Three peaks were identified for all samples; where for the BoL sample peak P1 had a maximum at 0.85 mAh cm^{-2}, peak P2 at 1.9 mAh cm^{-2}, and peak P3 at 2.9–3.7 mAh cm^{-2}. The final peak is inconsistent among the test cells and not used for further fitting. The corresponding reference peak capacities in mAh cm^{-2} (denoted Q_{P1} and Q_{P2}) are used to calculate characteristic peak spacings. Together with half-cell capacity (Q_d), they are marked in Figs. 8a, 8b. The changes in key peak spacings and capacity for electrodes harvested from the cells cycled at various conditions are shown in Figs. 8b, 8c in both mAh cm^{-2} and % of BoL values. Degradation of NCA results in changes of both the position of the peaks Q_{Pn} (where n is number of the peak) as well as its relative quantity. Such quantities have previously been defined and tracked over ageing for similar cells.[12,45]

In modelling of cell balancing and post mortem analysis, LAM is typically represented as a uniform scaling of the electrode potential profile[20,21] (and, proportionally, the differential voltage profile) with fewer redox centers, less charge compensation and, therefore, decreased capacity. This uniform view of LAM_{PE} presents a proportional decrease in all positive electrode peak spacings in DVA and in the observed discharge capacity. However, in this study, the first peak spacing, $Q_{P1} - 0$ for the aged samples (Fig. 8b, is far out of proportion when compared to Q_d. Electrodes from the cells cycled at 45 °C have particularly low values. The dramatic decrease in $Q_{P1} - 0$ represents that a very little capacity is available from the first reduction reaction during the lithiation of the aged NCA (①). On the other hand, the quantities $Q_{P2} - Q_{P1}$ and $Q_d - Q_{P2}$ (Fig. 8c), representing subsequent sections of the discharge curve, are much more consistent and in proportion with one another. Observing proportionality among the remainder of the DV profile, we suggest the spacing $Q_{P2} - Q_{P1}$ as a better candidate for accurately estimating the thermodynamic LAM_{PE}. That represents the expected loss of capacity in the absence of rate limitation. This quantity removes artifacts arising from the switch between charge and discharge and is presented also in SI Table SVI. The quantity $Q_d - Q_{P2}$ may also be suitable, though it should include kinetic limitations at the end of discharge that may be coupled with limitations of the lithium foil counter electrode.

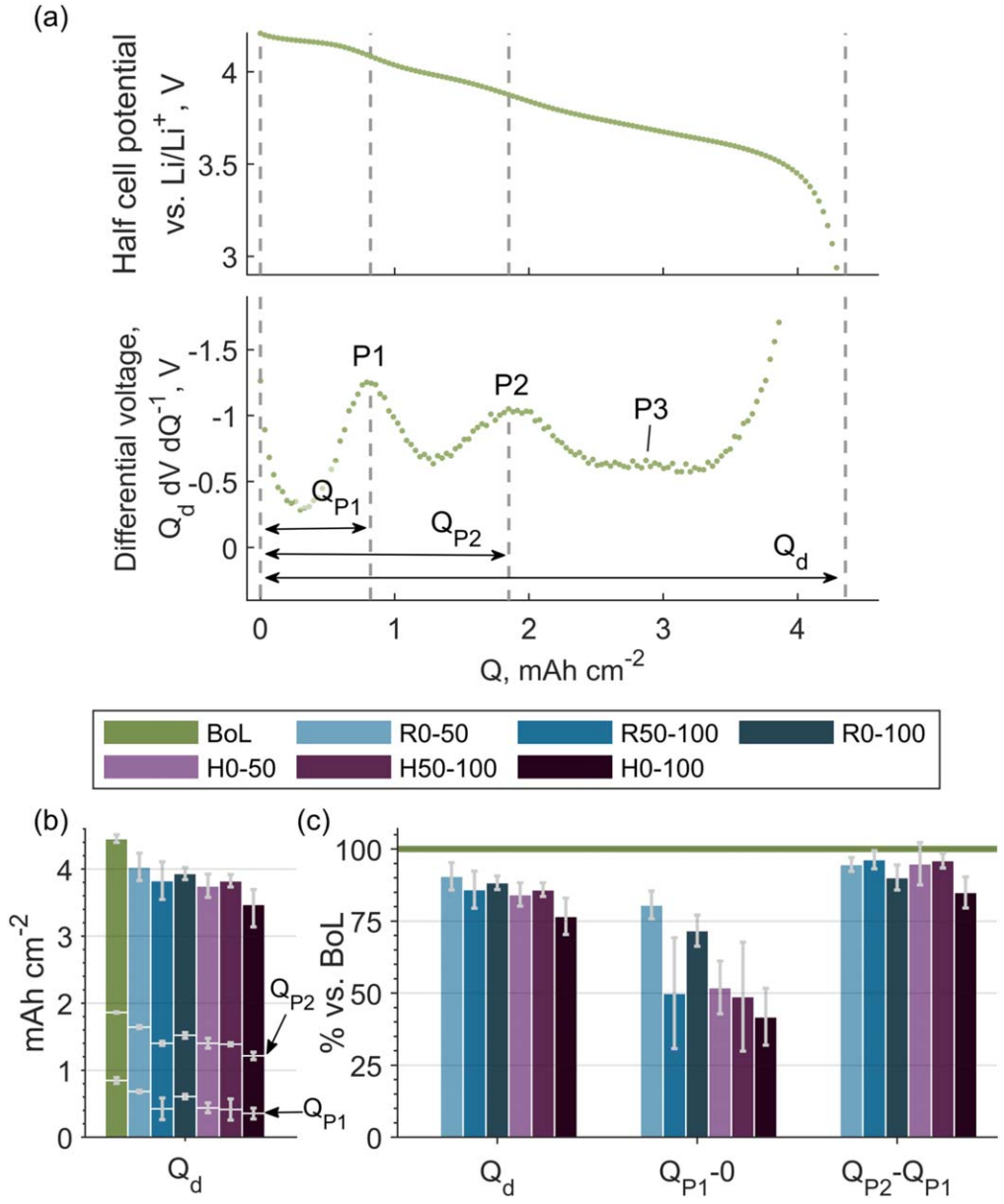

Figure 8. DVA analysis of the positive electrodes extracted from Regions 4 and 5: representative BoL half-cell potential and differential voltage profile of NCA/Li with characteristic peaks, spacings, and half-cell capacity marked (a); summary of capacity and DVA peak fitting (b) and selected values compared to BoL (c).

Figure 9 depicts cross-sectional SEM images of the positive electrode from fresh (Fig. 9a) and 0%–100% SoC aged at 45 °C (Fig. 9b) cells. Examination of the secondary particle microstructure reveals no significant particle cracking at 0% SoC, even under the most severe ageing conditions. However, in the aged cell voids within larger particles are visible, and in more detail a few particles exhibit cracking in their centers (SEM images for each cell are shown in SI Table SII). A slightly larger intergranular spacing is observed in aged electrodes. The evaluation of cathode thickness shows an average increase of 13%, with a higher increase of 17% for electrodes cycled between 50%–100% SoC (SI Table SIV). These results agree with previous studies that has shown partially reversible cracking in NCA,[69] including also the BoL material harvested from the cells presented here.[47] Furthermore, a surface layer (sometimes called the cathode-electrolyte interphase or CEI) and decomposition products is visible on all samples except for BoL and EoL aged at 22 °C 50%–100% SoC and 45 °C 0%–50% SoC (BoL and H0–100 cases are presented in SI Fig. S7). The CEI thickness (around 200 nm corresponding to only to 0.3% of the BoL active material thickness) cannot, however, account for the increase in the electrode volume. Therefore, the increase of the electrode thickness might be attributed to the particle voids seem to form inside the NCA particles, and those may be a part of the irreversible material expansion.

The formation of a rocksalt surface layer on the active material particles has been associated with an increase in resistance in lithium-ion batteries.[66] To investigate whether this phenomenon is relevant in the studied case, scanning transmission electron microscopy (STEM) was used to evaluate the formation of surface layers on fresh and aged electrodes. Figure 10 displays STEM images of the surface of NCA particles from both the BoL and the most severely aged EoL (H0–100) samples. Surprisingly, no rocksalt layer was detected on the surface of NCA particles in any of the samples (a and b correspondingly). To further investigate possible NCA surface inhomogeneity, the distribution of Ni was evaluated by EDS over the TEM samples of EoL samples, as shown in (Figs. 10c and 10d). No gradient of Ni concentration was observed, indicating that no deviating surface layers were observed on the particles and hence this phenomenon cannot be responsible for any significant increase in resistance in these samples. Additionally, the nanoporosity is clearly present in EoL (H0–100) electrodes and visible in Fig. 10d, which we address in a future study.

To better understand the structural changes in the bulk of the positive electrodes of lithium-ion batteries upon ageing, an XRD study was performed on powders extracted from the electrodes of both BoL and EoL cells. Rietveld refinement of this XRD data is presented in Table II. Changes in the lattice parameters a and c, and the ratio between them generally indicate structural changes in the electrode material. Additionally, the I_{003}/I_{104} ratio can be used to detect Ni/Li cation mixing,[70–72] which occur when the material deviates from hexagonal symmetry towards cubic symmetry, and a threshold value of 1.2 is often used to indicate this phenomenon.[70,73,74]

The results of the XRD analysis indicate that there is a minor shift in the c lattice parameter in the studied samples, with an EoL maximum deviation of 0.2% from the BoL sample. This deviation is significant, considering that the c lattice parameter usually deviates by approximately 1% during a delithiation within the stability region (up to 4.18 V full cell potential).[47] Notably, all cells cycled to high state of charge (R50–100, R0–100, H50–100, H0–100) have the same lattice parameter deviation at the same temperatures. As for the H0–50, it is the highest difference to BoL cell. Moreover, the c/a ratio remains close to the BoL values in all studied cases, showing that the structure preserved the same stability. The I_{003}/I_{104} ratios of the aged electrode are also relatively close to the BoL values, except for the samples cycled between 50%–100% SoC at 22 °C and 45 °C, which show lower values, close to 1.2. This indicate that the active material may experience a higher cation mixing in the upper SoC region. Overall, the XRD results suggest that the material is not reaching complete relithiation in cells cycled beyond 50% SoC at both temperatures (and H0–50) and suggested greater cation mixing for the samples cycled higher than 50% SoC.

The dissolution of transition metals is another common phenomenon observed in Ni-rich layered cathode materials.[75,76] Here, an elemental analysis evaluation of the positive electrode was performed using ICP-OES to investigate the dissolution of transition metals. However, direct comparison of transition metal ratios may be misleading as it may neglect a correlated, net change in all of the transition metals. To avoid this, the negative electrodes from the corresponding part of the positive electrode were analyzed since the dissolved transition metals are expected to be reduced on the negative electrode.[77] The amount of Ni detected in the negative electrode coating of BoL and EoL cells are presented in Fig. 11. A comparison of BoL and EoL cells showed that, although there was a relatively large variation between samples, a greater Ni content was observed in the negative electrodes of cells cycled between 50%–100% SoC. Furthermore, ageing at 45 °C resulted in higher Ni dissolution and deposition on the negative electrodes compared to ageing at 22 °C. The ICP-OES of the positive electrode was rather similar, and no further conclusions drawn from the data, see SI Figs. S10 and S11.

Detailed analysis of the degradation of the negative electrode.— For the negative electrode, DVA was also performed to determine the extent of its loss of active material on the negative electrode (LAM_{NE}) and to decouple the contributions from graphite and silicon oxide. The capacity of the graphite part of the active material was partitioned into three segments based on the sharp differential voltage peaks N1 and N3, illustrated in Fig. 12a. If kinetic limitations can be reasonably neglected (i.e., if cycling sufficiently

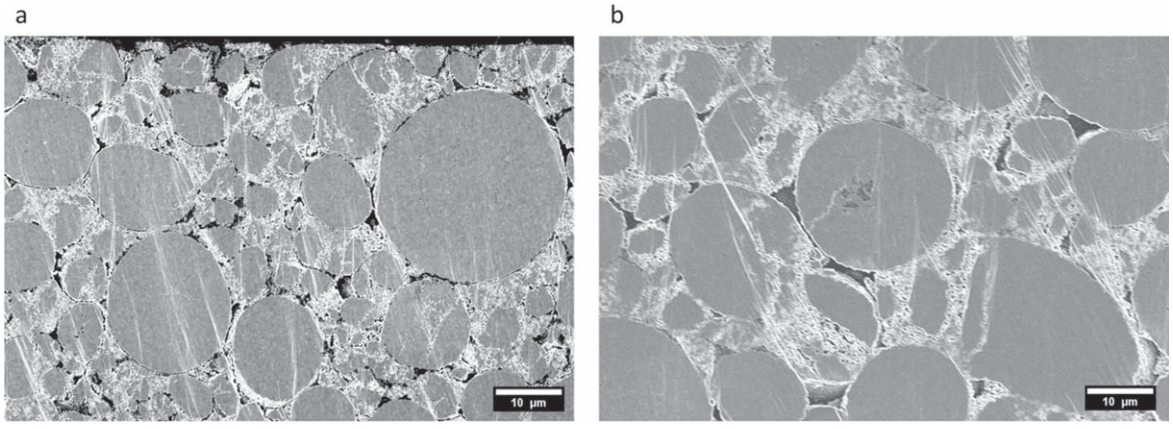

Figure 9. Cross-section SEM images of positive electrode: (a)—fresh cell; (b)—aged within 0–100% SoC at 45 °C cell.

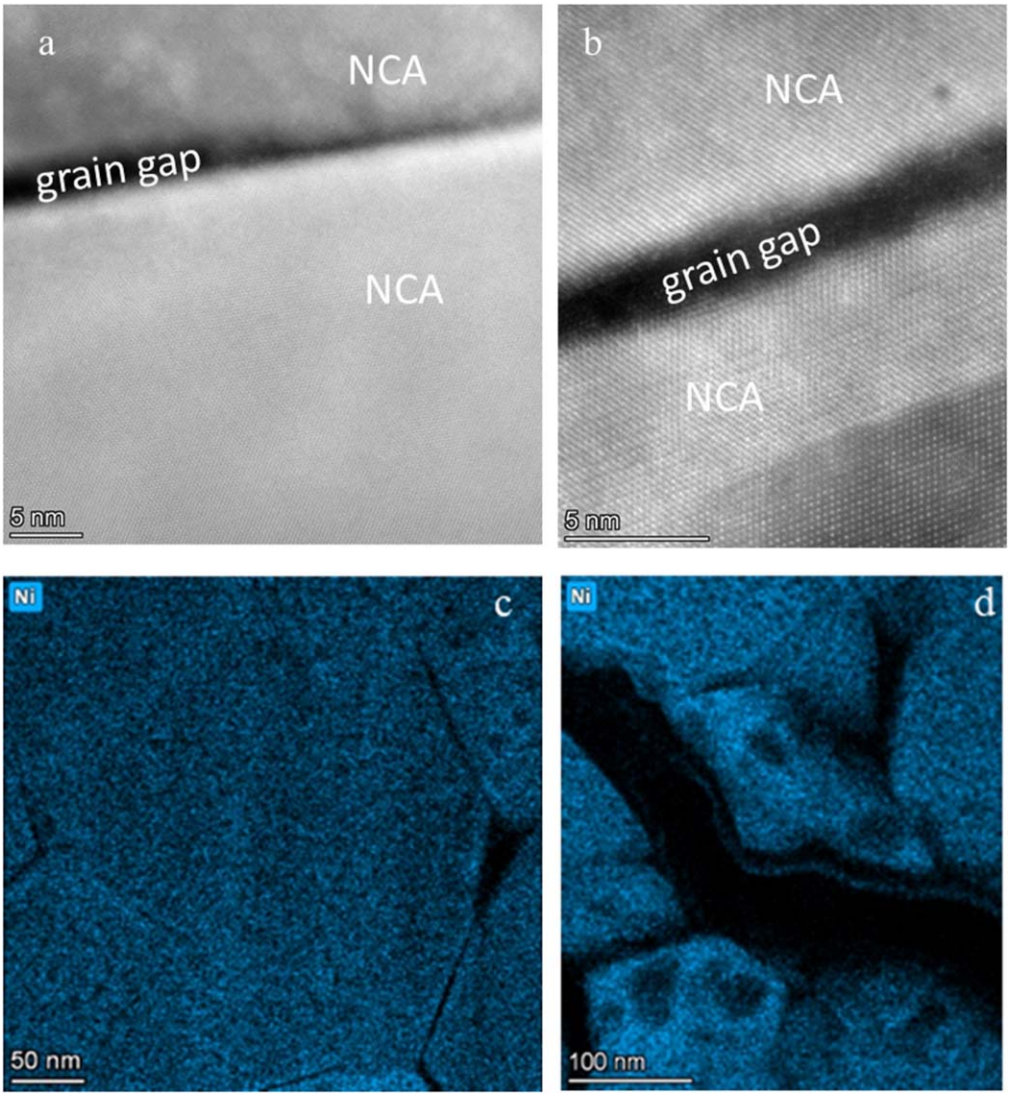

Figure 10. TEM images of the electrodes extracted from fresh (a) and aged within 0–100% SoC at 45 °C (b) cells together with EDS mapping of Ni done for BoL and EoL H0–100 electrodes (c) and (d) correspondingly.

Table II. X-ray diffraction results conducted over the powders extracted from positive electrodes at 0% SoC.

Sample	a, Å	c, Å	Δc, %	c/a	I_{003}/I_{104}
BoL	2.86160(3)	14.2464(3)	—	4.9785 (1)	1.316
R0–50	2.84837(6)	14.2410(6)	0.04	4.9997 (2)	1.382
R50–100	2.85500(4)	14.2771(5)	0.22	5.0007 (2)	1.186
R0–100	2.85416(5)	14.2781(5)	0.22	5.0026 (2)	1.292
H0–50	2.85216(4)	14.2900(4)	0.31	5.0102 (2)	1.389
H50–100	2.85618(4)	14.2731(4)	0.19	4.9989 (2)	1.269
H0–100	2.85623(3)	14.2732(3)	0.19	4.9972 (1)	1.378

slowly), the resulting segments a ($Q_{N1} - 0$), b ($Q_{N3} - Q_{N1}$), and c ($Q_d - Q_{N1}$) contain 50, 38, and 12% of the graphite capacity, respectively.[59,78,79] The observed capacities in each region, as well as the total electrode delithiation capacity, Q_d, is presented for each cycling condition in Fig. 12 and Table SVII (shown in SI) as the averages from multiple harvested electrodes from various regions within each test cell. Even in the blended electrode, region b, quantified as $Q_{N3} - Q_{N1}$, purely represents graphite activity with no contribution from the silicon fraction nor kinetic limitations. From the $Q_{N3} - Q_{N1}$ quantity, we can therefore estimate the total capacity of the graphite in the blended electrode, Q_{Gr}, where θ is the fraction of the thermodynamic graphite capacity in the respective region.

$$Q_{Gr} = \frac{Q_{N3} - Q_{N1}}{\theta_b}$$

Q_{Gr} values are calculated at BOL and EOL for each ageing case and presented in Fig. 12. Q_{Gr} serves as a quantitative metric of close-to-thermodynamic LAM_{Gr}. Knowing the effective graphite capacity, it is possible to deconvolute the activity of silicon from that of the

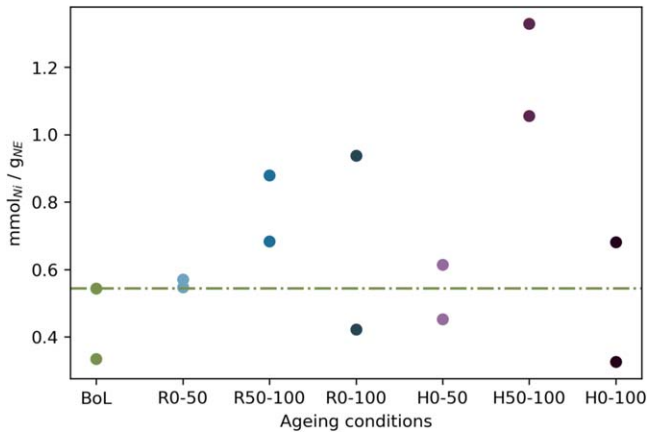

Figure 11. Ni detected in negative electrodes of BoL and EoL cells aged 0–50, 50–100 and 0%–100% SoC and two temperatures: 22 °C (R0–50, R50–100, R0–100) and 45 °C (H0–50, H50–100, H0–100).

dilute graphite stages at low extents of lithiation. This is achieved by subtracting the expected graphite contribution ($\theta_c \cdot Q_{\mathrm{Gr}}$) from the remaining capacity in region c.

$$Q_{\mathrm{Si}} = Q_d - Q_{\mathrm{N3}} - \theta_c \cdot Q_{\mathrm{Gr}}$$

The necessary assumption in this estimation is that both the silicon and graphite are fully delithiated following the 0.1C step to 1.5 V. Effectively, this resolves the silicon amount that is kinetically available, which may be somewhat less than the total silicon content determined by other techniques. In spirit, this method of separating the silicon contribution is the same as can be done with fitting the open circuit potential for blended electrodes.[80] However, this manual algebraic calculation provides simplified, quick quantification in concert with the analysis of the differential voltage profiles. The high SoC kinetic limitations can also be evaluated. In the early stage of delithiation, the underutilization of the graphite is represented by Q_{ul}. Similar to $Q_{P1} - 0$ for the positive electrodes, this underlithiation can be due to kinetic limitations on the previous charge step, or isolated regions that have poor conductive connection.

$$Q_{ul} = \theta_a \cdot Q_{\mathrm{Gr}} - Q_{\mathrm{N1}}$$

The key to these measurements is that they, like in our case, must be slow enough so that the electrode approaches pseudo-OCP and peaks N1 and N3 are sharp and can be confidently fitted. Increasing heterogeneity within the electrodes can smear out these peaks, making such measurements particularly challenging at full-cell level, as remarked in our parallel cycling study on narrow SoC windows.[17]

The evaluation of BoL electrodes reveals that silicon initially contributes 17% (0.72 mAh cm^{-2}) of the achievable capacity of 4.3 mAh cm^{-2}. Ultimately, in the various ageing cases, 45%–72% of this silicon capacity is lost, compared to a maximum of a few percent capacity loss of the graphite. In some cases, the graphite capacity even increases by EoL, though this is within the standard deviation among cells. This can be attributed to kinetic improvements with mild exfoliation and increases in the interlayer spacing of graphite.[68] Overall, the stability of Q_{Gr} suggests that graphite has had minimal impact on capacity fade in these cells. For each SoC range, the cells cycled at 22 °C retained 5%–10% more silicon capacity than their counterparts cycled at higher temperature. However, the 22 °C cells attained greater values of Q_{ul}, indicating greater kinetic limitations or more trapped lithium, though this value has greater variation among the test cells. Regardless, we suggest that the difference of the graphite behavior at various temperatures is tied to greater utilization of the graphite in the 45 °C-cycled electrodes (having less active silicon). Even though the silicon degradation was severe in all cases, it was the least so for those cells cycled 50%–100% SoC (R50–100 and H50–100), indicating that time spent in lower cell voltage region was more detrimental for the silicon. It is noted that the cells cycled at high SoC still over the cell lifetime had several full cell cycles (from 0 to 100% SoC) during 30+ RPTs, and that this may have contributed, to some degree, to the observed losses of SiO_x capacity.

A comparison of the negative electrode cross-section SEM images from samples harvested at BoL and EoL are shown in Fig. 13. EDS mapping was done to differentiate surfaces of SiO_x and graphite (SI Fig. S8). The SEM images revealed an 11.6% increase in the electrode coating thickness in aged cells within the 0%–50% and 0%–100% SoC ranges. This finding can be attributed to the expansion of the electrode during cycling. In addition to the thickness change, the morphology of the silicon (Si) particles in the electrodes also exhibited distinct differences between BoL and EoL cells, as evidenced by the SEM images shown in Fig. 13. The morphology of Si-containing particles was found to differ with respect to the temperature range of the cycled electrodes (SI Table SIII). Specifically, an extensive development of a loose morphology around the particles upon ageing (Fig. 13). Changes in morphology in the coating layer were also observed (Figs. 13c, 13d). At higher magnification, the SEM images of the EoL sample also showed that the entire SiO_x particle was porous, with pore sizes in the range of tens of nanometers (Fig. 13e). Furthermore, the growth of SEI around SiO_x particle was dendritic and displayed a compositional gradient, as evidenced by the image contrast (Fig. 13e).

The electrodes thickness increase was measured (Table SV in SI). The samples operated at high temperature and had cut-off at low SoC have demonstrated the most significant expansion (samples H0–50 and H0–100). Interestingly, the same samples developed loose morphology. In each temperature set, the samples operated at high SoC (R50–100 and H50–100) have demonstrated the lowest thickness increase. The observed change might correlate with expansion of SiO_x particles which are more affected at low SoC and higher temperature.

Discussion

The starting point for the study is an analysis of the ICA of the fresh and aged cylindrical cells during their ageing process in order to identify ageing modes (Fig. 3). Regardless of cycling conditions, some of the peaks associated with both positive and negative electrodes disappear (Fig. 3), which is attributed both to LAM and LLI. These results also show that SiO_x electrochemical activity is decreased for the cells that are cycled down to 0% SoC such as R0–50, H0–50, R0–100, and H0–100 (Figs. 3b, 3c, 3f, 3g). This trend is expected as SiO_x is known to degrade at cell potentials below 50% SoC.[80] On the contrary, the positive electrode degradation is anticipated at potentials corresponding to ⩾50% SoC due to lower stability of the positive electrode upon delithiation.[81] The electrochemical activity of NCA was seen to decrease significantly for the cells cycled at 45 °C and up to 100% SoC (Figs. 3e, 3g).

The ICA results indicated heterogeneous degradation. This was later confirmed with post mortem analysis (Fig. 4). Spatially inhomogeneous degradation is a known phenomenon and depends on distributions of temperature, pressure, and electrolyte in the battery cells.[37,62,82] It is worth mentioning that in the studied cases this heterogeneity is present but yet not severe enough to lead to the "knee point" which is typical for cells exhibiting a higher degree of ageing heterogeneity.[55] The general trend across all ageing conditions shows a sublinear dependence of capacity loss vs the number of FCE (Fig. 2). It is generally proposed that such dependence is typical for the cells where degradation is mostly due to the side reactions.[55] The side reactions that occur usually take place consuming Li^+ ions resulting in LLI. Li^+ ions are typically lost in SEI formation, electrolyte decomposition and other side reactions which coincide with general ageing trends observed in cycling of the studied full cells. Most of the capacity fade attributable to LLI is a consequence of electrode slippage, i.e., a gradually increasing

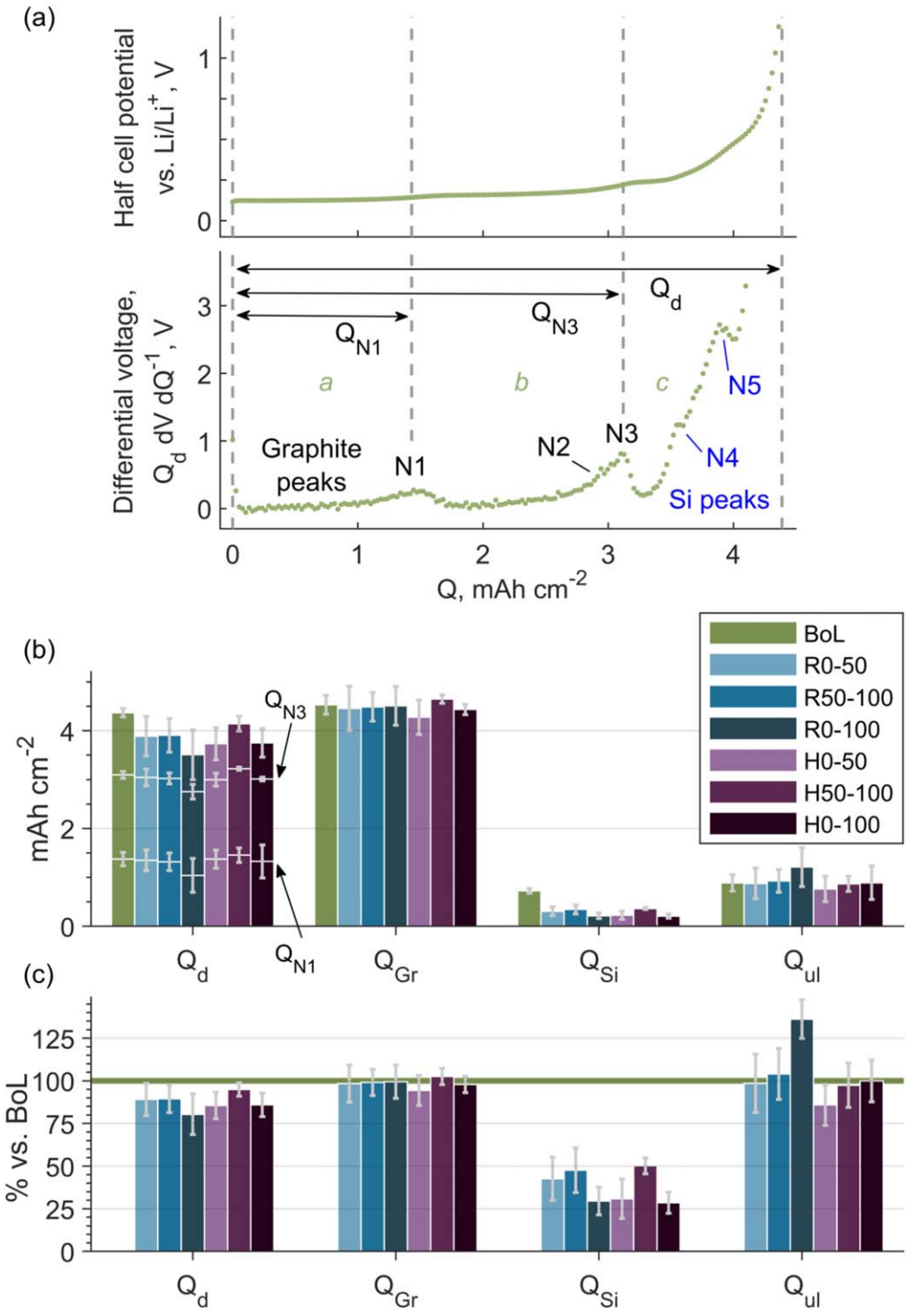

Figure 12. DVA of the negative electrodes extracted from Regions 4 and 5: representative BoL half-cell potential and differential voltage profile of Gr-SiO_x/Li with graphite and silicon peaks and important capacities marked (a); summary of calculated values from DVA peak fitting (b) and calculated values compared to BoL (c). Error bars represent the standard deviation among all test cells for each case.

mismatch in electrode-level SoC that results in underutilization of the electrodes. Consideration of LLI in the electrolyte is also important, however, as Li^+ is present in excess in the electrolyte, the effect has a lesser extent. In the current study, LLI was quantified post mortem and was found to be similar in all conditions and was confirmed as the main cause for the loss of capacity, on the order of $\sim$1 mAh cm^{-2}. The LLI being very similar in the samples cycled at different conditions might be a result of the samples analyzed at similar capacity loss state. The data suggests that LLI is the limiting mechanism for the capacity loss. Therefore, the difference in the capacity loss rate might be related to the difference in the LLI rate due to various ageing conditions.

Together with LLI, LAM is known to be a significant source of the cell degradation.[24,25] LAM evaluation was conducted for both positive and negative electrodes. The positive electrode has shown 15% of LAM_{PE} on average and similar for most cases within statistical error (Table SVI in SI). However, when the kinetic limitations are isolated and removed in half-cell DVA, the average

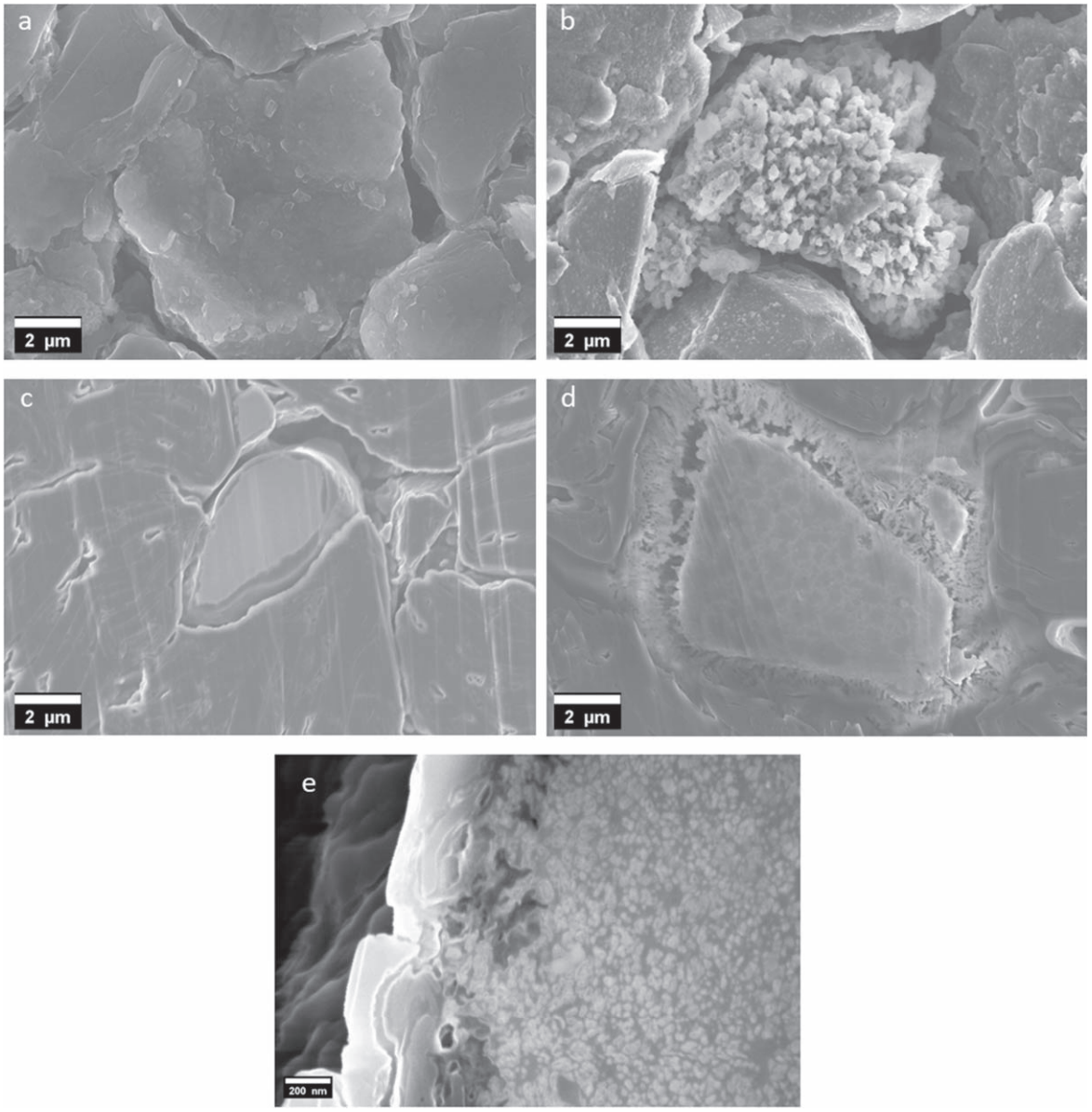

Figure 13. SEM images of SiO_x particles in fresh and aged electrodes: (a)—top view of BoL negative electrode; (b)—top view of H0–100 negative electrode; (c)—cross section view of BoL negative electrode; (d)—cross section view of H0-100 negative electrode; (e)—higher magnification of cross section view of SiO_x particle.

figure for thermodynamic LAM decreases to 7.2%. Thermodynamic LAM_{PE} is higher for ageing in full SoC range (R0–100 and H0–100). Understanding the LAM_{PE} extent was done using post mortem electrochemical characterization of the electrodes in a half-cell configuration. The ex situ capacity evaluation of the electrode contribution indicated prevalent ageing of the negative electrode under most conditions and the positive electrode at 45 °C cycled between 50–100 and 0%–100% SoC. The Li-ion diffusion resistance coefficient k can indicate whether there are kinetic limitations within the active material. In our study, k increases from the narrow range (cells cycling within 50% Depth of Discharge) to the full range (cell cycling within full SoC) and higher k at higher temperature for most conditions (Fig. 7).

Further, we address various mechanisms of LAM_{PE}. LAM_{PE} unites processes such as particle cracking resulting in inactivation of particles, transition metal dissolution, and phase transitions to less electrochemically-active phases together with oxygen release.[29] From ex situ studies, it is seen that high-temperature cycling affects the loss of active material more significantly.[11] The study of oxygen evolution on materials extracted from the same BoL cell has been conducted previously by our group, showing CO_2 evolution as a result of reactions involving lattice oxygen and electrolyte.[47] The cells cycled between 50%–100% SoC and 0%–100% SoC have shown the presence of voids in larger particles (Fig. 9 and SI Table SII). Particle cracking was evaluated for EoL samples and found present to a lesser extent than is generally discussed in the literature.[69,83] It might be related to presence of W, grain boundary engineering and the development of nanopores inside the primary particles, which act to decrease the strain within the secondary particles. Instead, voids were found in the center of larger particles. Similar features have been previously reported for NMC and NCA.[69,84] However, the cross-section study does not provide sufficient statistics on whether it is present for the entire sample due to the technique limitation. Our previous study conducted on BoL samples has also showed visible upon material delithiation yet reversible upon relithiation cracking.[47]

A loss of active material into inactive phases was not observed by means of XRD nor TEM. The BoL and EoL samples have similar

lattice parameters (Table II). The rock salt phase, to which the capacity loss and Li diffusion resistance increase is often attributed, was not observed neither for BoL nor for EoL samples (Fig. 7). TEM EDX also confirmed the Ni distribution to be homogeneous (Fig. 7, and no inhomogeneous structure within primary particles was found, consistent with previously reported results.[85] However, the Rietveld refinement disclosed a difference in lattice parameters as well as indicated cationic mixing which can influence Li diffusion resistance.[86–88] Additionally, the thickness of the CEI and decomposition products visible with electron microscopy does not correlate with higher values of k.

LAM_{PE} as a result of transition metal dissolution was identified through increased Ni concentration in negative electrodes samples upon ageing. It is possible that HF etching may induce Ni dissolution and migration from the positive electrode.[76] The Ni dissolution is significant in cells cycled within 50%–100% SoC in both temperatures and increased at 45 °C, which may be attributed to the higher number of cycles with these cells. The high-temperature cell (H0–100) and room-temperature cell (R0–100) completed 1950 and 2570 FCE respectively compared to ∼800–1000 FCE performed by the rest of the cells. These results agree with previously observed trends for Ni-rich layered oxide cathodes (NMC811).[75] This indicates that the level of Ni dissolution might be correlated to the time the active materials operated within high SoC.

Similarly to the LAM_{PE} study, LAM_{NE} was analyzed. The average thermodynamic LAM_{NE} of the aged, blended electrodes overall is 9.7%. Here, in the blended electrode, the graphite loss was found to be insignificant. XRD of the negative electrode supports this conclusion (SI Fig. S12). At the same time, the loss of active SiO_x is shown to be around 60% on average. However, comparing the LAM_{NE} of cells aged in different conditions is challenging because the difference between ageing conditions of the most values are within the statistical error which can be attributed to heterogeneity within the cell. It indicates an importance of accounting for statistics in this kind of analysis.

SEM study of the negative electrode has shown development of pores within the SiO_x particles as well as a significant change in the particle surface which may result in Li trapping and electrical isolation.[89] Si particles are well-known for their surface reactivity.[90] A change in the morphology of the SiO_x particle surface was observed at 45 °C for cells reaching 0% SoC while cycling and it might be one of the sources causing a significant change of k for high-temperature aged negative electrodes. Lithium diffusion resistance trends indeed show a slight increase of k for negative electrodes aged at 22 °C (Fig. 7 and a significant increase when aged at 45 °C between 0%–50% SoC.

The investigation of RI degradation mode, which affects power density of the cells, was out of the scope of the current study. However, we noted several sources which can contribute it. The ICP results have shown higher presence of the Cu in the negative electrode coating with a higher amount in the samples aged between 50–100 and 0–100 for both high and room temperatures (Fig. S8 in SI). That indicates greater collector corrosion in these conditions which is one of the RI sources. Additionally, the separator was investigated for pore reduction (SI Fig. S13) and we have shown a significant change in the EoL sample which can cause a higher cell resistance by reducing ion conductivity.[29]

The study conducted on post mortem samples was analyzed for contributions introduced from cell disassembly. The SEM images showed no delamination of the active material from the current collector after taking the electrodes apart and mechanically removing one side (SI Fig. S9). However, the comparison of ICI measured on the full cell (SI, Fig. S14) and half cells from extracted electrodes (Fig. 7) has shown that the values of the lithium diffusion coefficient have increased almost threefold (∼3.4 $\Omega\ s^{-0.5}\,cm^2$ measured in full cell compared to ∼10.1 $\Omega\ s^{-0.5}\,cm^2$ calculated as the sum of the k measured in half cells). Here, the influence of the double contribution of the separator as well as less optimized cell geometry in addition to a much lower current used in the case of the full cell plays a substantial role. Yet, an evaluation of the contributions of each step to achieve an understanding regarding the artefacts it may contribute is essential for these types of studies.

Cell geometry-dependent ageing has been also studied as it plays a significant role in cell degradation.[91] Interestingly, the positive electrode material experiences higher capacity loss in regions of higher temperature.[92] The ageing within the cell roll complies with trends reported earlier with higher degradation towards the outer part of the cell.[37] Based on the degradation trends observed in the positive and negative electrodes, it can be seen that when one electrode exhibits higher levels of degradation, the opposite electrode tends to experience a comparatively lower degree of aging.

Although the present study extensively explores the degradation mechanisms, it is essential to acknowledge its limitations. The study primarily concentrates on the degradation mechanisms of LAM and examines the processes occurring within the bulk of the material. As a result, the study only provides limited coverage of SEI-related processes and the degradation of inactive cell components. The latter will be a key focus of future work.

Conclusions

In summary, a comprehensive investigation of ageing in EV cells was carried out. By subjecting the cells to two different temperatures and three different SoC ranges, a thorough analysis of their long-term cycling performance was performed. The results demonstrated that LLI is a major factor in capacity loss and can be associated with degradation products deposited at both the positive and negative electrodes as well as extensive development of a dendritic SEI on the SiO_x particles. The latter played a crucial role in the capacity loss observed on the negative electrode in the studied cells. With the growing popularity of the blended negative electrodes in the commercial batteries, it demonstrates the limits of such batteries' lifetime would be highly dependent on the degradation of SiO_x and emphasize importance to consider it in the future design of the blended electrodes. The LAM_{PE} was found to be particularly prominent at higher operating cell potentials. Void formation within the secondary particles was observed as well as indications of cation mixing. The positive electrode ageing mechanisms were found to be enhanced at elevated temperatures. The analysis also identified other, often overlooked factors, contributing to resistance increase, such as separator ageing and dissolution of the copper current collector. The study was done by a holistic approach creating an extensive understanding of the degradation mechanisms in the relevant commercial EV cells. A wide range of methods was used to support the study: electrochemical (galvanostatic cycling of full and half-cells, ICI), structural (XRD), microscopy (SEM, TEM), and compositional (ICP, EDS) analyses. Additionally, the in-depth analysis such as DVA was used to understand the individual contribution of blended electrode compounds to the ageing (i.e., loss of SiO_x over graphite). These findings have both academic and industrial relevance suggesting valuable aspects to consider for the future electrode design and cell operating conditions.

Acknowledgments

The authors acknowledge Bertrand Philippe for providing the cells for the current study and Olivier Donzel-Gargand for FIB preparation of the samples. We acknowledge Myfab Uppsala for providing facilities and experimental support. Myfab is funded by the Swedish Research Council (2019-00207) as a national research infrastructure. We also acknowledge the financial support from the Swedish Energy Agency to the project "Ageing of Lithium-ion Batteries with Nickel-Rich Cathodes for Electromobility" (project number: 45538-1) as well as StandUP for Energy consortium, Sweden. This work was performed, in part, at the Electron Microscopy Centre, supported by the Department of Materials and Environmental Chemistry and Faculty of Science at Stockholm University, Sweden.

ORCID

Anastasiia Mikheenkova https://orcid.org/0000-0002-5845-3403
Alexander J. Smith https://orcid.org/0000-0003-1321-6639
Kristian B. Frenander https://orcid.org/0000-0002-4929-1051
Cheuk-Wai Tai https://orcid.org/0000-0001-7286-1211

References

1. J. Conzade et al., *Why the Automotive Future Is Electric* (2022), [Online]. Available: (https://mckinsey.com/industries/automotive-and-assembly/our-insights/why-the-automotive-future-is-electric).
2. IEA, *World Energy Model* (IEA, Paris) (2021), [Online]. Available: (https://iea.org/reports/world-energy-model).
3. C. Fetting, *The European Green Deal*, (ESDN Office, Vienna) (2020).
4. J. Store, "Fit for 55 package: Council reaches general approaches relating to emissions reductions and their social impacts." *European Council* (2022), Accessed: Sep. 25, 2022. [Online]. Available: (https://consilium.europa.eu/en/press/press-releases/2022/06/29/fit-for-55-council-reaches-general-approaches-relating-to-emissions-reductions-and-removals-and-their-social-impacts/).
5. D. Stampatori, P. P. Raimondi, and M. Noussan, "Li-ion batteries: a review of a key technology for transport decarbonization." *Energies*, **13**, 10 (2020).
6. M. Weil, S. Ziemann, and J. Peters, "The issue of metal resources in li-ion batteries for electric vehicles." *Behaviour of Lithium-Ion Batteries in Electric Vehicles: Battery Health, Performance, Safety, and Cost*, ed. G. Pistoia and B. Liaw (Green Energy and Technology: Springer International Publishing, Cham), p. 59 (2018).
7. C. Xu, Q. Dai, L. Gaines, M. Hu, A. Tukker, and B. Steubing, "Future material demand for automotive lithium-based batteries." *Commun. Mater.*, **1**, 1 (2020).
8. X. Lai et al., "Critical review of life cycle assessment of lithium-ion batteries for electric vehicles: A lifespan perspective." *eTransportation*, **12**, 100169 (2022).
9. H. Wang, S. Frisco, E. Gottlieb, R. Yuan, and J. F. Whitacre, "Capacity degradation in commercial Li-ion cells: The effects of charge protocol and temperature." *J. Power Sources*, **426**, 67 (2019).
10. M.-K. Tran, A. DaCosta, A. Mevawalla, S. Panchal, and M. Fowler, "Comparative study of equivalent circuit models performance in four common lithium-ion batteries: LFP, NMC, LMO, NCA." *Batteries*, **7**, 51 3 (2021).
11. Y. Preger et al., "Degradation of commercial lithium-ion cells as a function of chemistry and cycling conditions." *J. Electrochem. Soc.*, **167**, 120532 (2020).
12. P. Keil and A. Jossen, "Calendar aging of NCA lithium-ion batteries investigated by differential voltage analysis and coulomb tracking." *J. Electrochem. Soc.*, **164**, A6066 (2017).
13. M. Kemeny, P. Ondrejka, and M. Mikolasek, "Comprehensive degradation analysis of NCA li-ion batteries via methods of electrochemical characterisation for various stress-inducing scenarios." *Batteries*, **9**, 33 1 (2023).
14. E. Wikner, E. Björklund, J. Fridner, D. Brandell, and T. Thiringer, "How the utilised SOC window in commercial Li-ion pouch cells influence battery ageing." *J. Power Sources Adv.*, **8**, 100054 (2021).
15. M. Schindler, J. Sturm, S. Ludwig, A. Durdel, and A. Jossen, "Comprehensive analysis of the aging behavior of nickel-rich, silicon-graphite lithium-ion cells subject to varying temperature and charging profiles." *J. Electrochem. Soc.*, **168**, 060522 (2021).
16. F. Benavente-Araoz, M. Varini, A. Lundblad, S. Cabrera, and G. Lindbergh, "Effect of partial cycling of NCA/graphite cylindrical cells in different SOC intervals." *J. Electrochem. Soc.*, **167**, 040529 (2020).
17. N. Roy Chowdhury et al., (2023), Manuscript in preparation.
18. X. Liu et al., "Bridging multiscale characterization technologies and digital modeling to evaluate lithium battery full lifecycle." *Adv. Energy Mater.*, **12**, 2200889 (2022).
19. M. Jafari, K. Khan, and L. Gauchia, "Deterministic models of Li-ion battery aging: It is a matter of scale." *J. Energy Storage*, **20**, 67 (2018).
20. M. Dubarry, C. Truchot, and B. Y. Liaw, "Synthesize battery degradation modes via a diagnostic and prognostic model." *J. Power Sources*, **219**, 204 (2012).
21. C. R. Birkl, M. R. Roberts, E. McTurk, P. G. Bruce, and D. A. Howey, "Degradation diagnostics for lithium ion cells." *J. Power Sources*, **341**, 373 (2017).
22. A. Barré, B. Deguilhem, S. Grolleau, M. Gérard, F. Suard, and D. Riu, "A review on lithium-ion battery ageing mechanisms and estimations for automotive applications." *J. Power Sources*, **241**, 680 (2013).
23. S. Sarkar, S. Z. Halim, M. M. El-Halwagi, and F. I. Khan, "Electrochemical models: methods and applications for safer lithium-ion battery operation." *J. Electrochem. Soc.*, **169**, 100501 (2022).
24. H. Sun et al., "Quantitative analysis of degradation modes of lithium-ion battery under different operating conditions." *Energies*, **14**, 350 2 (2021).
25. E. Sarasketa-Zabala, F. Aguesse, I. Villarreal, L. M. Rodriguez-Martinez, C. M. López, and P. Kubiak, "Understanding lithium inventory loss and sudden performance fade in cylindrical cells during cycling with deep-discharge steps." *J. Phys. Chem. C*, **119**, 896 (2015).
26. X. Kong, A. Bonakdarpour, B. T. Wetton, D. P. Wilkinson, and B. Gopaluni, "State of health estimation for lithium-ion batteries." *IFAC-Pap.*, **51**, 667 (2018).
27. G. Seo et al., "Rapid determination of lithium-ion battery degradation: High C-rate LAM and calculated limiting LLI." *J. Energy Chem.*, **67**, 663 (2022).
28. B. Rowden and N. Garcia-Araez, "Estimating lithium-ion battery behavior from half-cell data." *Energy Rep.*, **7**, 97 (2021).
29. J. S. Edge et al., "Lithium ion battery degradation: what you need to know." *Phys. Chem. Chem. Phys.*, **23**, 8200 (2021).
30. J. Vetter et al., "Ageing mechanisms in lithium-ion batteries." *J. Power Sources*, **147**, 269 (2005).
31. M. Armand et al., "Lithium-ion batteries—Current state of the art and anticipated developments." *J. Power Sources*, **479**, 228708 (2020).
32. P. Teichert, G. G. Eshetu, H. Jahnke, and E. Figgemeier, "Degradation and aging routes of ni-rich cathode based li-ion batteries." *Batter.*, **6**, 8 (2020).
33. O. Capron, R. Gopalakrishnan, J. Jaguemont, P. Van Den Bossche, N. Omar, and J. Van Mierlo, "On the ageing of high energy lithium-ion batteries—comprehensive electrochemical diffusivity studies of harvested nickel manganese cobalt electrodes." *Materials*, **11**, 176 (2018).
34. R. Jung, M. Metzger, F. Maglia, C. Stinner, and H. A. Gasteiger, "Oxygen release and its effect on the cycling stability of LiNixMnyCozO2(NMC) cathode materials for li-ion batteries." *J. Electrochem. Soc.*, **164**, A1361 (2017).
35. S.-M. Bak et al., "Structural changes and thermal stability of charged LiNixMnyCozO2 cathode materials studied by combined in situ time-resolved XRD and Mass Spectroscopy." *ACS Appl. Mater. Interfaces*, **6**, 22594 (2014).
36. K. Kleiner et al., "On the microscopic origin of reversible and irreversible reactions of LiNixCoyMnx cathode materials: Ni–O hybrid bond formation vs cationic and anionic redox." (2020), Accessed: Dec. 17, 2021. [Online]. Available: (https://arxiv.org/abs/2006.09964v1).
37. M. Uitz et al., "Aging of Tesla's 18650 lithium-ion cells: correlating solid-electrolyte-interphase evolution with fading in capacity and power." *J. Electrochem. Soc.*, **164**, A3503 (2017).
38. E. Peled and S. Menkin, "Review—SEI: past, present and future." *J. Electrochem. Soc.*, **164**, A1703 (2017).
39. J. T. Frith, M. J. Lacey, and U. Ulissi, "A non-academic perspective on the future of lithium-based batteries." *Nat. Commun.*, **14**, 420 1 (2023).
40. A. Mikheenkova et al., *Ageing of High Energy Density Automotive Li-ion Batteries: The Effect of Temperature and State-of-Charge* (2023).
41. S. Solchenbach, D. Pritzl, E. J. Y. Kong, J. Landesfeind, and H. A. Gasteiger, "A gold micro-reference electrode for impedance and potential measurements in lithium ion batteries." *J. Electrochem. Soc.*, **163**, A2265 (2016).
42. Y.-C. Chien, H. Liu, A. S. Menon, W. R. Brant, D. Brandell, and M. J. Lacey, "Rapid determination of solid-state diffusion coefficients in Li-based batteries via intermittent current interruption method." *Nat. Commun.*, **14**, 2289 1 (2023).
43. M. J. Lacey, K. Edström, and D. Brandell, "Visualising the problems with balancing lithium-sulfur batteries by 'mapping' internal resistance." *Chem. Commun.*, **51**, 16502 (2015).
44. Y. Li et al., "A quick on-line state of health estimation method for Li-ion battery with incremental capacity curves processed by Gaussian filter." *J. Power Sources*, **373**, 40 (2018).
45. A. J. Smith, P. Svens, M. Varini, G. Lindbergh, and R. W. Lindström, "Expanded in situ aging indicators for lithium-ion batteries with a blended NMC-LMO electrode cycled at sub-ambient temperature." *J. Electrochem. Soc.*, **168**, 110530 (2021).
46. T. O'Haver, *Interactive Peak Fitter (ipf.m)*, (The University of Maryland at College Park) (2017).
47. A. Mikheenkova, O. Gustafsson, C. Misiewicz, W. R. Brant, M. Hahlin, and M. J. Lacey, "Resolving high potential structural deterioration in Ni-rich layered cathode materials for lithium-ion batteries operando." *Journal of Energy Storage*, **57**, 106211 (2023).
48. A. A. Coelho, "TOPAS and TOPAS-Academic: an optimization program integrating computer algebra and crystallographic objects written in C++." *J. Appl. Crystallogr.*, **51**, 210 (2018).
49. R. Schröder, M. Aydemir, and G. Seliger, "Comparatively assessing different shapes of lithium-ion battery cells." *Procedia Manuf.*, **8**, 104 (2017).
50. R. Zhang, H. Qiu, and Y. Zhang, "Enhancing the electrochemical performance of Ni-Rich LiNi0.88Co0.09Al0.03O2 cathodes through tungsten-doping for lithium-ion batteries." *Nanomaterials*, **12**, 729 (2022).
51. J. Schmitt, M. Schindler, and A. Jossen, "Change in the half-cell open-circuit potential curves of silicon–graphite and nickel-rich lithium nickel manganese cobalt oxide during cycle aging." *J. Power Sources*, **506**, 230240 (2021).
52. G. Sharma, Y. Jin, and Y. S. Lin, "Lithium ion batteries with alumina separator for improved safety." *J. Electrochem. Soc.*, **164**, A1184 (2017).
53. Z. Liu et al., "Safer lithium-ion batteries from the separator aspect: development and future perspectives." *ENERGY Environ. Mater.*, **4**, 336 (2021).
54. S. Klein et al., "Understanding the role of commercial separators and their reactivity toward LiPF6 on the failure mechanism of high-voltage NCM523 || graphite lithium ion cells." *Adv. Energy Mater.*, **12**, 2102599 (2022).
55. P. M. Attia et al., "Review—'knees' in lithium-ion battery aging trajectories." *J. Electrochem. Soc.*, **169**, 060517 (2022).
56. H. Li et al., "An unavoidable challenge for ni-rich positive electrode materials for lithium-ion batteries." *Chem. Mater.*, **31**, 7574 (2019).
57. K.-J. Park, H.-G. Jung, L.-Y. Kuo, P. Kaghazchi, C. S. Yoon, and Y.-K. Sun, "Improved cycling stability of Li[Ni0.90Co0.05Mn0.05]O2 through microstructure modification by boron doping for li-ion batteries." *Adv. Energy Mater.*, **8**, 1801202 (2018).
58. D. Anseán, G. Baure, M. González, I. Cameán, A. B. García, and M. Dubarry, "Mechanistic investigation of silicon-graphite/LiNi0.8Mn0.1Co0.1O2 commercial cells for non-intrusive diagnosis and prognosis." *J. Power Sources*, **459**, 227882 (2020).
59. D. Aurbach, B. Markovsky, I. Weissman, E. Levi, and Y. Ein-Eli, "On the correlation between surface chemistry and performance of graphite negative electrodes for Li ion batteries." *Electrochim. Acta*, **45**, 67 (1999).
60. J. Sieg et al., "Local degradation and differential voltage analysis of aged lithium-ion pouch cells." *J. Energy Storage*, **30**, 101582 (2020).

61. J. Li, J. Harlow, N. Stakheiko, N. Zhang, J. Paulsen, and J. Dahn, "Dependence of cell failure on cut-off voltage ranges and observation of kinetic hindrance in LiNi0.8Co0.15Al0.05O2." *J. Electrochem. Soc.*, **165**, A2682 (2018).
62. M. J. Mühlbauer et al., "Inhomogeneous distribution of lithium and electrolyte in aged Li-ion cylindrical cells." *J. Power Sources*, **475**, 228690 (2020).
63. J. Christensen and J. Newman, "Cyclable lithium and capacity loss in li-ion cells." *J. Electrochem. Soc.*, **152**, A818 (2005).
64. Z. Geng, T. Thiringer, and M. J. Lacey, "Intermittent current interruption method for commercial lithium-ion batteries aging characterization." *IEEE Trans. Transp. Electrification*, **8**, 2985 (2022).
65. Z. Geng, Y. C. Chien, M. J. Lacey, T. Thiringer, and D. Brandell, "Validity of solid-state Li+ diffusion coefficient estimation by electrochemical approaches for lithium-ion batteries." *Electrochim. Acta*, **404**, 139727 (2022).
66. C. Xu et al., "Bulk fatigue induced by surface reconstruction in layered Ni-rich cathodes for Li-ion batteries." *Nat. Mater.*, **20**, 84 (2021).
67. H. Gao, Q. Wu, Y. Hu, J. P. Zheng, K. Amine, and Z. Chen, "Revealing the rate-limiting Li-Ion diffusion pathway in ultrathick electrodes for li-ion batteries." *J. Phys. Chem. Lett.*, **9**, 5100 (2018).
68. J. Guo, Y. Li, J. Meng, K. Pedersen, L. Gurevich, and D.-I. Stroe, "Understanding the mechanism of capacity increase during early cycling of commercial NMC/graphite lithium-ion batteries." *J. Energy Chem.*, **74**, 34 (2022).
69. K. J. Park et al., "Degradation mechanism of ni-enriched NCA cathode for lithium batteries: are microcracks really critical?" *ACS Energy Lett.*, **4**, 1394 (2019).
70. X. Zhang, W. J. Jiang, A. Mauger, Qilu, F. Gendron, and C. M. Julien, "Minimization of the cation mixing in Li1+x(NMC)1−xO2 as cathode material." *J. Power Sources*, **195**, 1292 (2010).
71. J. Zheng et al., "Ni/Li disordering in layered transition metal oxide: electrochemical impact, origin, and control." *Acc. Chem. Res.*, **52**, 2201 (2019).
72. J. Li, L. E. Downie, L. Ma, W. Qiu, and J. R. Dahn, "Study of the failure mechanisms of LiNi0.8Mn0.1Co0.1O2 cathode material for lithium ion batteries." *J. Electrochem. Soc.*, **162**, A1401 (2015).
73. Y. Koyama, N. Yabuuchi, I. Tanaka, H. Adachi, and T. Ohzuku, "Solid-state chemistry and electrochemistry of LiCo1/3Ni1/3Mn1/3 O 2 for advanced lithium-ion batteries: i. first-principles calculation on the crystal and electronic structures." *J. Electrochem. Soc.*, **151**, A1545 (2004).
74. J. Morales, C. Pérez-Vicente, and J. L. Tirado, "Cation distribution and chemical deintercalation of Li1-xNi1+xO2." *Mater. Res. Bull.*, **25**, 623 (1990).
75. Z. Ruff, C. Xu, and C. P. Grey, "Transition metal dissolution and degradation in NMC811-graphite electrochemical cells." *J. Electrochem. Soc.*, **168**, 060518 (2021).
76. R. Jung et al., "Nickel, manganese, and cobalt dissolution from Ni-Rich NMC and their effects on NMC622-graphite cells." *J. Electrochem. Soc.*, **166**, A378 (2019).
77. T. Joshi, K. Eom, G. Yushin, and T. F. Fuller, "Effects of dissolved transition metals on the electrochemical performance and SEI growth in lithium-ion batteries." *J. Electrochem. Soc.*, **161**, A1915 (2014).
78. Q. Zhang, Q. Guo, and R. E. White, "A new kinetic equation for intercalation electrodes." *J. Electrochem. Soc.*, **153**, A301 (2005).
79. J. Z. Olson, C. M. López, and E. J. F. Dickinson, "Differential analysis of galvanostatic cycle data from li-ion batteries: interpretative insights and graphical heuristics." *Chem. Mater.*, **35**, 1487 (2023).
80. N. Kirkaldy, M. A. Samieian, G. J. Offer, M. Marinescu, and Y. Patel, "Lithium-ion battery degradation: measuring rapid loss of active silicon in silicon–graphite composite electrodes." *ACS Appl. Energy Mater.*, **5**, 13367 (2022).
81. T. Li, X.-Z. Yuan, L. Zhang, D. Song, K. Shi, and C. Bock, *Degradation Mechanisms and Mitigation Strategies of Nickel-Rich NMC-Based Lithium-Ion Batteries* (Springer, Singapore) Vol. 2018 (2019).
82. Y. Xie et al., "Inhomogeneous degradation induced by lithium plating in a large-format lithium-ion battery." *J. Power Sources*, **542**, 231753 (2022).
83. T. M. M. Heenan et al., "Identifying the origins of microstructural defects such as cracking within Ni-rich NMC811 cathode particles for lithium-ion batteries." *Adv. Energy Mater.*, **10**, 2002655 (2020).
84. R. Xu et al., "Heterogeneous damage in Li-ion batteries: Experimental analysis and theoretical modeling." *J. Mech. Phys. Solids*, **129**, 160 (2019).
85. B. Wang et al., "Which of the nickel-rich NCM and NCA is structurally superior as a cathode material for lithium-ion batteries?" *J. Mater. Chem. A*, **9**, 13540 (2021).
86. S. S. Zhang, "Problems and their origins of Ni-rich layered oxide cathode materials." *Energy Storage Mater.*, **24**, 247 (2020).
87. K. Luo et al., "Charge-compensation in 3d-transition-metal-oxide intercalation cathodes through the generation of localized electron holes on oxygen." *Nat. Chem.*, **8**, 684 (2016).
88. D. H. Seo, J. Lee, A. Urban, R. Malik, S. Kang, and G. Ceder, "The structural and chemical origin of the oxygen redox activity in layered and cation-disordered Li-excess cathode materials." *Nat. Chem.*, **8**, 692 (2016).
89. T. Kwon, J. W. Choi, and A. Coskun, "The emerging era of supramolecular polymeric binders in silicon anodes." *Chem. Soc. Rev.*, **47**, 2145 (2018).
90. M. Wetjen, S. Solchenbach, D. Pritzl, J. Hou, V. Tileli, and H. A. Gasteiger, "Morphological changes of silicon nanoparticles and the influence of cutoff potentials in silicon-graphite electrodes." *J. Electrochem. Soc.*, **165**, A1503 (2018).
91. T. Waldmann, R. G. Scurtu, K. Richter, and M. Wohlfahrt-Mehrens, "18650 vs 21700 Li-ion cells—A direct comparison of electrochemical, thermal, and geometrical properties." *J. Power Sources*, **472**, 228614 (2020).
92. Z. Wang, J. Ma, and L. Zhang, "Finite element thermal model and simulation for a cylindrical li-ion battery." *IEEE Access*, **5**, 15372 (2017).